Mode structure and ray dynamics of a parabolic dome microcavity

Jens U. Nöckel

Max-Planck-Institut für Physik komplexer Systeme, Nöthnitzer Strasse 38, 01187 Dresden, Germany

Guillaume Bourdon, Eric Le Ru, Richard Adams, Isabelle Robert, Jean-Marie Moison, and Izo Abram

Laboratoire CDP CNRS/CNET, 196 Avenue Henri Ravera, F-92220 Bagneux, France

(Received 4 April 2000)

We consider the wave and ray dynamics of an electromagnetic field in a parabolic dome microcavity. The structure of the fundamental *s* wave involves a main lobe in which the electromagnetic field is confined around the focal point in an effective volume of the order of a cubic wavelength, while modes with finite angular momentum have a structure that avoids the focal area and have correspondingly larger effective volumes. The ray dynamics indicate that the fundamental *s* wave is robust with respect to small geometrical deformations of the cavity, while the higher order modes are unstable, giving rise to optical chaos. We discuss the incidence of these results on the modification of the spontaneous emission dynamics of an emitter placed in such a parabolic dome microcavity.

PACS number(s): 42.25.−p, 42.55.Sa, 05.45.Mt, 05.45.Ac

I. INTRODUCTION

The miniaturization of optoelectronic devices such as light-emitting diodes or semiconductor lasers is expected to lead to an improvement of their energy efficiency, and to a lowering of the lasing threshold. This tendency toward miniaturization has led to the exploration of optical microcavities whose dimensions are of the order of a few wavelengths [1]. In such microcavities the extreme confinement of the electromagnetic field modifies the interaction of the active medium with the radiation field, so that the process of spontaneous emission is altered both in its spatial and dynamical characteristics. Spontaneous emission can thus be redirected, enhanced, or inhibited in a way that may be exploited for the operation of light-emitting diodes or lasers. A modification of the characteristics of spontaneous emission, such as its directionality or the emission rate, was shown for several microcavity designs such as for the traditional Fabry-Perot planar cavities [2] and for disk-shaped [3] or spherical [4] cavities displaying whispering gallery modes.

One of the key requirements for enhancing the dynamics of spontaneous emission and reducing the laser threshold is that the electromagnetic field at the site of the emitting dipole should be enhanced inside the cavity with respect to its value in free space. A class of resonators for which this can be achieved very efficiently is that of confocal cavities: A few experiments with spherical confocal cavities [5], or semiconfocal microcavities [6] were reported already, in which significant spontaneous emission modification or extremely low laser thresholds were observed. Among the different designs of concave mirrors, *parabolic* mirrors have an important advantage in that their focal point displays no astigmatism, and is free from spherical aberrations. Basic geometric optics thus leads us to expect that double-parabolic confocal cavities or planoparabolic semiconfocal cavities should display a strong enhancement of the electromagnetic field in the vicinity of the focal point, and a concomitant modification of the emission characteristics of an active medium placed there.

This paper presents a theoretical analysis of microcavities formed by a parabolic mirror at or close to the confocal condition. The study is motivated by experimental work in which such a system has in fact been fabricated. The experimental characterization of the modal structure and dynamics, now in progress, will be given in a separate publication [7]. Here we briefly describe the experimental structure, in order to define the system for which our model calculations are intended. We have fabricated a semiconfocal planoparabolic semiconductor microcavity (see Fig. 1) by etching an appropriately prepared GaAs wafer by a focused ion beam [8] to produce a ''hill'' of cylindrical symmetry and parabolic vertical cross section having a diameter of 7.2 μm and a height of 1.8 μm [corresponding to optical lengths of 27λ and 6.75λ respectively, for a wavelength (*in vacuo*) of 960 nm] which was subsequently covered with a thin metallic layer of
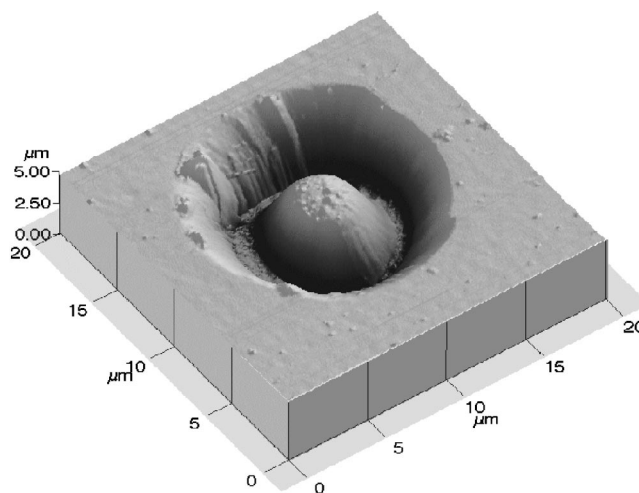

FIG. 1. Atomic force microscope image of a ''hill'' of diameter 7.2 μm and a parabolic cross section of height 1.8 μm, etched on a GaAs substrate by a focused ion beam apparatus. When covered with gold this constitutes a concave parabolic mirror, with its focal point inside the GaAs substrate.
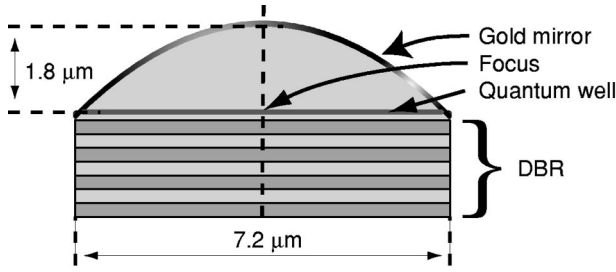
FIG. 2. Schematic cross section of a semiconfocal parabolic dome cavity, consisting of a parabolic gold mirror and a planar Bragg mirror placed at the focal plane of the parabola. The cavity spacer is made of GaAs, and the light emitter is a quantum well placed in the vicinity of the focal plane.

gold. This gold dome constituted thus a concave parabolic mirror with its focal point inside the GaAs substrate. At the base of the parabolic hill, the wafer had a six-period GaAs/AlAs Bragg mirror, closing the semiconfocal cavity (see Fig. 2). This cavity is expected to possess a mode in which the electric field is strongly enhanced in the vicinity of the focal point, so that a localized semiconductor emitter, such as a quantum box or quantum well, emitting at a wavelength near 960 nm, will have its spontaneous emission greatly enhanced when placed there. The use of a dielectric mirror with a lower refractive index rather than a metallic mirror at the focal plane is important because it introduces a boundary condition that requires the tangential electric field to be maximal at the focal plane. This condition cannot be fulfilled on a metallic mirror, on which the tangential electric field should vanish, thus producing a vanishing field at the focal point of the parabola.

In order to understand the operation of such a cavity, and to assess its performance in modifying spontaneous emission, in this paper we first examine the modal structure of an ideal confocal double-parabolic, or semiconfocal planoparabolic, microcavity. We then investigate the stability of these modes with respect to geometric deformations of the cavity that correspond to deviations from confocality; this condition is inevitably violated in a realistic cavity due to fabrication defects. The discussion of this case provides a conceptual and theoretical background for the experimental analysis to be presented in a subsequent paper.

The calculation of the modal structure of the parabolic dome microresonators cannot be treated within the paraxial approximation of conventional [9] resonator theory, because of the very large aperture displayed by the parabola and because the cavity dimensions are comparable to the optical wavelength. Extensions of the paraxial approximation to highly convergent (or divergent) beams produced by parabolic mirrors are cumbersome even in macroscopic resonators [10], where the optical axis is long compared with the wavelength—in microresonators, the latter breaks down as well. However, there are other approximate techniques which are well suited to the problem we consider. As a valuable tool for simplifying the exact solution of Maxwell's equations for the cavity modes, we employ a short-wavelength approximation leading to simple WKB quantization conditions. The assumption that wavelengths are much shorter than the relevant cavity dimensions is common to both WKB and paraxial approximations, and it is therefore

surprising at first sight that the WKB approach yields an excellent quantitative agreement with the exact cavity spectrum even for the longest-wavelength modes of the parabolic cavity. We show how this arises by discussing in detail the structure of the classical ray dynamics in the resonator which makes the WKB approximation possible. As a result, we shall then also be able to assess the stability of the modal structure with regard to fabrication imperfections, based on a ray analysis for parabolic cavities in cases where confocality is violated. To characterize the modes of the parabolic resonator, the internal caustic structure formed by the rays turns out to be of crucial importance. These considerations establish a connection between the the microcavity optics of the paraboloic dome and the field of quantum chaos: even minute deviations from confocality introduce chaos into the ray dynamics, and we have to address the significance of this effect for the relevant cavity modes.

The paper is organized as follows: Sec. II, introduces the mathematical model that describes confocal parabolic cavities, while Sec. III presents the wave equation for the electromagnetic field in cylindrical and parabolic coordinates, and discusses its exact vectorial and scalar solutions. Section IV presents the WKB approximation of the wave equations for the parabolic cavity, an approach that in Sec. VI will permit us to make a connection with ray optics, while Sec. V compares the numerical solutions of the wave equations in the parabolic microcavity with those of the WKB approximation. Section VI introduces the main concepts of ray optics applied to our parabolic cavities with cylindrical symmetry, while Sec. VII analyzes the stability of the ray trajectories in a parabolic cavity in which there is a slight deviation from confocality. Section VIII discusses the problem of the finite acceptance angle of Bragg mirrors, a feature that limits the lifetime of modes in semiconfocal cavities bounded by such mirrors. Finally, Sec. IX summarizes the results of this study, and gives its conclusions.

II. MODEL

We consider a model structure for an ideal semiconfocal cavity which is bounded by a metallic concave parabolic mirror on one side and a planar dielectric mirror on the other side, placed at the focal plane of the parabola. In cylindrical coordinates (ρ, z, ϕ), the parabolic mirror is given by

$$z = f - \frac{\rho^2}{4f}, \tag{1}$$

where f is the focal distance of the parabola, while the focal plane (and the planar mirror) corresponds to

$$z = 0. \tag{2}$$

It is convenient to describe this cavity in parabolic coordinates (ξ, η, ϕ), whose properties are summarized in the Appendix. For reference, here we reproduce the transformation to cylindrical coordinates as given in Eq. (A3):

$$\rho = \sqrt{\xi \eta},$$
$$\tag{3}$$
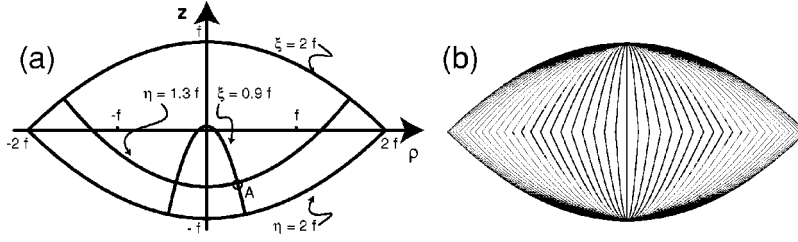$$z = \tfrac{1}{2} (\xi - \eta).$$

FIG. 3. (a) Representation of parabolic cylinder coordinates in the z-ρ plane of a cylindrical coordinate system (z is the vertical axis). The third dimension is obtained by rotating the figure around $\hat{z}$ by the angle ϕ. Point A is specified by $\xi=1.3f$, $\eta=0.9f$, and $\phi=0$. The focus of all parabolas is at the origin. (b) By unfolding the parabolic dome into a double paraboloid, the boundary conditions on the common focal plane can be restated as simple parity requirement under reflection at this plane ($z=0$). For TE modes, the electric field must be even under this reflection. The unfolded cavity is shown in side view with meridians which make 90° corners at the focal plane. The latter is also the equatorial plane of the cavity.

To illustrate this coordinate system, in Fig. 3(a) we show how the intersection of the coordinate surfaces defines a point A in the plane z versus ρ. Also shown is the cavity shape itself: the parabolic mirror corresponds to

$$\xi=2f, \qquad (4)$$

and the planar dielectric mirror is at

$$\xi=\eta. \qquad (5)$$

In an ideal cavity, the parabolic metallic mirror can be assumed to be lossless, displaying an amplitude reflectivity $r=-1$. This produces a π phase change upon reflection so that it corresponds to a boundary condition in which the tangential electric field vanishes. In parabolic coordinates this can be expressed as

$$E_\eta(\xi=2f)=0, \quad E_\phi(\xi=2f)=0, \quad B_\xi(\xi=2f)=0. \quad (6)$$

Similarly, the planar dielectric mirror can be assumed to have a reflectivity of $r=+1$, producing no phase change upon reflection, so that the tangential magnetic field vanishes on the focal plane of the cavity. In cylindrical coordinates, this can be expressed as

$$B_\rho(z=0)=B_\phi(z=0)=0, \quad E_z(z=0)=0. \qquad (7)$$

Alternatively, this implies that the tangential electric field is maximum on the focal plane, and is symmetric under reflection of the whole cavity at the $z=0$ plane. Thus, instead of considering this plane as an additional boundary with properties (7), one can *unfold* the cavity across this plane by reflection, to obtain a confocal double paraboloid shown in Fig. 3(b). This extended cavity requires only the metallic boundary conditions on its parabolic walls, that is Eq. (6) and its equivalent, in which ξ and η are interchanged. It will support modes that can be either symmetric or antisymmetric under reflection at the focal plane. If we restrict ourselves to modes in which E_ρ and E_ϕ are symmetric, this subset is identical to the modes of the original dome with the conditions of Eqs. (6) and (7).

The advantage of considering the unfolded cavity is that the focal plane as a physical boundary drops out of the discussion; this will considerably simplify the interpretation in terms of the ray picture later on. Therefore, in the remainder of this paper, we can refer to Fig. 3(b) as our model system.

III. WAVE EQUATION

The electric field $\vec{E}$ obeys the vectorial wave equation

$$\nabla\times\nabla\times\vec{E}+\mu\epsilon\frac{\partial^2\vec{E}}{\partial t^2}=0 \qquad (8)$$

under the additional constraint that its divergence must vanish:

$$\nabla\cdot\vec{E}=0. \qquad (9)$$

The boundary conditions and the constraint of zero divergence imposed on the electromagnetic field in general will lead to a coupling between the various vectorial components of the electric and magnetic fields. In simpler geometries such as cylinders, spheres, or rectangular cavities, a suitable choice of polarizations reduces the problem to finding the eigensolutions of a scalar Helmholtz equation [11], However, in our case the three polarizations and the intersecting parabolic surfaces forming the resonator cannot be labeled by the coordinate lines of a single orthogonal coordinate system, as is possible in the textbook systems mentioned. We now discuss the implications of this complication.

A. Vector field components in cylindrical coordinates

After combining Eqs. (8) and (9) to the wave equation,

$$\nabla^2\vec{E}-\mu\epsilon\frac{\partial^2\vec{E}}{\partial t^2}=0, \qquad (10)$$

we can take advantage of the cylindrical symmetry of the problem by expressing the wave equation for a time-harmonic electric field oscillating at frequency ω in cylindrical coordinates (ρ,z,ϕ), as

$$\nabla^2 E_\rho-\frac{1}{\rho^2}E_\rho-\frac{2}{\rho^2}\frac{\partial E_\phi}{\partial\phi}+\mu\epsilon\omega^2 E_\rho=0, \qquad (11a)$$

$$\nabla^2 E_\phi-\frac{1}{\rho^2}E_\phi+\frac{2}{\rho^2}\frac{\partial E_\rho}{\partial\phi}+\mu\epsilon\omega^2 E_\phi=0, \qquad (11b)$$

$$\nabla^2 E_z+\mu\epsilon\omega^2 E_z=0. \qquad (11c)$$

We note that the wave equation couples the radial and angular components of the electric field (E_ρ and E_ϕ), while the equation for the axial component E_z is scalar. One can achieve a further simplification in this system of equations as follows:

The rotational symmetry around the z axis permits us to assume a ϕ dependence of all components of the field of the form

$$Q(\rho, z)e^{im\phi}. \tag{12}$$

With this ansatz, Eqs. (11a) and (11b) can be written as

$$\rho^2[\nabla^2 + k^2]E_\rho - E_\rho = 2imE_\phi, \tag{13a}$$

$$\rho^2[\nabla^2 + k^2]E_\phi - E_\phi = -2imE_\rho, \tag{13b}$$

where $k = \sqrt{\mu\epsilon}\,\omega$ is the wave number inside the parabolic dome. If the azimuthal quantum number $m = 0$, this reduces to two identical equations. If, on the other hand, $m \neq 0$, we can form a suitable linear combination of E_ρ and E_ϕ which decouples these two equations. Naively setting $E_\phi = 0$ would not achieve this goal, because it forces both field components to vanish.

The proper linear combination in which to decouple this system of differential equations is obtained with the definitions

$$E_\rho \equiv \frac{i}{\sqrt{2}}(E_+ - E_-),$$

$$\tag{14}$$

$$E_\phi \equiv \frac{1}{\sqrt{2}}(E_+ + E_-).$$

Then $E_\pm$ is the solution of the equation

$$\rho^2[\nabla^2 + k^2]E_\pm = (1 \pm 2m)E_\pm. \tag{15}$$

This definition again makes use of the azimuthal symmetry of the resonator, which implies that the circular polarizations $\hat{\sigma}_\pm = \mp i/\sqrt{2}(\hat{\rho} \pm i\hat{\phi})$ are decoupled in the cylindrical wave equation. In this way, we have therefore formally decoupled the original system of equations (11) for the vector field components. In the special case $m = 0$, cases E_+ and E_- will moreover be linearly dependent because their respective equations again coincide.

However, this decoupling of polarizations in the wave equation does not reduce the problem to a truly scalar one, because the field components are still coupled by the boundary conditions and by the condition of zero divergence. On the ''top'' parabolic mirror, conditions (6) in terms of the cylindrical components of the electric field at $\xi = 2f$ now read

$$i\sqrt{f}(E_+ - E_-) + \sqrt{\eta}E_z = 0,$$

$$E_+ + E_- = 0, \tag{16}$$

$$\frac{\partial}{\partial\eta}(E_+ + E_-) = 0.$$

The first line expresses the condition $E_\eta = 0$, and the second and third lines represent $E_\phi = 0$ and $B_\xi = 0$, respectively. On the ''bottom'' parabolic mirror the boundary conditions are the same as in Eq. (16), with ξ and η interchanged.

B. Absence of longitudinal electromagnetic modes

Unfortunately, the set of boundary conditions [Eqs. (16)] is not yet a complete list of constraints that we have to satisfy. An additional requirement is that the field at every point in the resonator has to have zero divergence, which in parabolic coordinates reads

$$E_+ - E_- + m(E_+ + E_-) + \frac{2\xi\eta}{\xi+\eta}\left(\frac{\partial}{\partial\xi} + \frac{\partial}{\partial\eta}\right)(E_+ - E_-)$$

$$+ \frac{2i\sqrt{2\xi\eta}}{\xi+\eta}\left(\xi\frac{\partial}{\partial\xi} + \eta\frac{\partial}{\partial\eta}\right)E_z = 0. \tag{17}$$

This assumption already entered into the derivation of the system of wave equation (10), from the original Maxwell equations in the form of Eq. (8). However, this does not guarantee that all solutions of Eqs. (10) or (11) satisfy Eq. (17). The latter is just the well-known statement that the electromagnetic field is purely *transverse*, ruling out longitudinal modes: the transverse electric field $\vec{E}_\perp$ is related to the curl of the magnetic field by the Maxwell equation

$$\nabla \times \vec{B} = \frac{1}{c}\frac{\partial\vec{B}}{\partial t} = ik\vec{E}_\perp, \tag{18}$$

and hence satisfies $\nabla \cdot \vec{E}_\perp = 0$; the longitudinal field $\vec{E}_\parallel$, which can be written as the gradient of a potential Φ, is responsible for violations of Eq. (17).

In view of the constraints imposed by the boundary conditions (16) and by the zero divergence condition (17) it is not possible (except for the case $m = 0$, as we shall see later) to set one (or two) of the vector components to zero without setting the full electric field identically to zero, and thus it is not possible to reduce in a rigorous manner the vector problem into a scalar one. The problem can in principle be solved by converting Eq. (17) from a condition in the cavity *volume* to a *boundary condition* which can then be treated on the same footing as Eqs. (16). One way of achieving this [12] is by noting that if

$$\vec{E}_0 \equiv \vec{E}_\perp + \vec{E}_\parallel \tag{19}$$

fulfills Eq. (10), then so does

$$\vec{E} \equiv k^2\nabla \times \nabla \times \vec{E}_0 = k^2\nabla \times \nabla \times \vec{E}_\perp. \tag{20}$$

The latter is automatically divergence free. In order for $\vec{E}$ to satisfy the boundary condition $\vec{E}_t = 0$, we require for $\vec{E}_0$ that

$$(\vec{E}_0)_t = 0 \quad \text{and} \quad \nabla \cdot \vec{E}_0 = 0 \tag{21}$$

on the surface. Then one indeed has

$$\vec{E}_t = k^2(\nabla \times \nabla \times \vec{E}_0)_t = k^2(\vec{E}_0 + \nabla(\nabla \cdot \vec{E}_0))_t = k^2(\vec{E}_0)_t = 0 \tag{22}$$

on the boundary. The problem is therefore reduced to finding the auxiliary field $\vec{E}_0$ and then deducing the transverse field from Eq. (21). This leads to a system of three second-order differential equations for each vector component of $\vec{E}_0$, given by Eq. (11), all of which are coupled by boundary conditions that are, however, quite complex.

The next step is then to write the field components as linear combinations of independent general solutions of Eq. (11), and determine the unknown coefficients in that expansion from the matching conditions at the boundary. The solution proceeds in an analogous but much less tedious way if we neglect the additional divergence condition. The important simplification is that we are then able to consider the E_+ and E_- components of the electric field independently, by setting all except for one component to zero. Boundary conditions (16) are then decoupled as well. More precisely, it will be shown that the wave equations are then not only scalar but also *separable*, i.e., reducible to the solution of ordinary differential equations.

We therefore would like to neglect the coupling that results from the condition of zero divergence, provided that this can be justified in the context of the present study. There are various reasons why this approximation will provide us with useful results. Foremost, it will turn out below that the most important modes we find in this way in fact conspire to satisfy Eq. (17) *a posteriori* (cf. Sec. III E): the modes that provide the best confinement of the field in a tightly focused region around the focal point are the ones with $m=0$. For these, the different vector components decouple rigorously, and the scalar program is exact. These $m=0$ modes are particularly significant because they provide the best confinement of the field in a tight focal volume. This is the paramount aim of the experimental dome structure.

In addition to this exact result, the more transparent simplified problem allows us to evaluate the stability of the stationary states of the field in the parabolic cavity with respect to deviations from the confocality condition—a deformation that can readily occur in the course fabrication. This will be addressed with the help of the ray picture in Sec. VII, and the ray trajectories themselves are independent of whether a vectorial or scalar field is considered. Since the exact nature of the deformation is unknown, it is necessary to make model assumptions and parametrize the deformation in some way. Although the range of possible behaviors explored within our model can be argued to be generic, we lose at that point the ability to predict accuratey all the individual modes of the specific sample. The error incurred by this fundamental uncertainty about the precise boundary shape is larger than the error made by adopting the simplified boundary conditions, and hence the latter are warranted on physical grounds.

The consistency of these arguments is proven in Sec. VII where we find that the only modes which *can* in fact be reliably predicted for a large range of possible deformations (because they are structurally stable against the emergence of chaos) are the ones with low m (or angular momentum in the classical picture), concentrated strongly near the z axis. For these modes one can set approximately $m \approx 0$, $E_+ = E_-$ and $E_z = 0$, so that Eq. (17) becomes valid.

C. Wave equation in parabolic coordinates

Having discussed the boundary conditions, we now provide the solutions to Eq. (15). In order to find a system of general solutions to the formally scalar differential equations, Eqs. (11c) or (15), we express the scalar Laplacian appearing there in parabolic coordinates (ξ, η, ϕ), leading to the form

$$\frac{4}{\xi+\eta}\left[\frac{\partial}{\partial\xi}\left(\xi\frac{\partial Q}{\partial\xi}\right)+\frac{\partial}{\partial\eta}\left(\eta\frac{\partial Q}{\partial\eta}\right)\right]+k^2Q=\frac{n^2}{\xi\eta}Q, \quad (23)$$

where

$$n=m+1 \quad \text{for } Q=E_+,$$
$$n=m-1 \quad \text{for } Q=E_-, \quad (24)$$
$$n=m \quad \text{for } Q=E_z.$$

Here we have used the fact that the derivative $\partial^2/\partial\phi^2$ appearing in the Laplacian ∇^2 pulls down a factor $-m^2$ due to the ansatz [Eq. (12)]. Although the right-hand side is the analog of the centrifugal barrier in cylindrical problems, it thus depends not on angular momentum m directly but on a modified azimuthal mode number n. This occurs due to the additional ϕ derivatives introduced when we transformed the vector field components to cylindrical coordinates in Eq. (11).

At this point we introduce the approximation of discarding the divergence condition, so that we merely have to consider boundary conditions (16) with one and only one of the three field components nonzero. Then Eq. (23) is separable in η and ξ. We shall return to the details of the solution procedure in Sec. IV; for now it is sufficient to give the result: Denoting the separation constant by β, the solution can be written in the form

$$Q=F(k,\beta,\xi)F(k,-\beta,\eta), \quad (25)$$

where $F(k,\beta,\xi)$ obeys

$$\xi F''+F'+\left(-\frac{n^2/4}{\xi}+\frac{k^2}{4}\xi+\beta\right)F=0. \quad (26)$$

The functions $F(k,\beta,\xi)$ and $F(k,-\beta,\eta)$ appearing here are solutions of this differential equation with the same k and n, but with sign-reversed β, and hence their functional dependence on ξ and η will be different unless $\beta=0$. Without loss of generality, we can assume n to be non-negative, because it appears in the above equation only as n^2. The solutions that do not diverge at $\xi=0$ are of the form

$$F(k,\beta,\xi)=e^{ik\xi/2}\xi^{n/2}M\left(\frac{n+1}{2}-\frac{i\beta}{k};n+1;-ik\xi\right), \quad (27)$$

where $M(a,b,z)$ is Kummer's confluent hypergeometric function. The function F as written here is in fact real, because of the Kummer transformation [13]

$$M\left(\frac{b}{2}-a,b,-z\right)=e^{-z}M\left(\frac{b}{2}+a,b,z\right), \quad (28)$$

where we set $a=i\beta/k$, $b=n+1$ and $z=ik\xi$. Appplying the theorem then yields $F(k,\beta,\xi)=F(k,\beta,\xi)^*$.

The separation constant β and the wave number k at which to find the mode are still unknowns of the problem that have to be determined from the boundary conditions. The first constraint we can write down is

$$F(k,\beta,2f) \equiv 0 \tag{29}$$

to enforce vanishing tangential field on the parabolic surface. In the two-dimensional plane spanned by the unknowns β and k, this single equation defines a set of curves. The boundary condition on the focal plane requires that $E_\pm$ be symmetric under reflection, i.e., invariant under $\xi \leftrightarrow \eta$. For E_z, on the other hand, one needs odd parity. In order to construct such solutions with a well-defined parity, we have to form linear combinations

$$E = F(k,\beta,\xi)F(k,-\beta,\eta) \pm F(k,-\beta,\xi)F(k,\beta,\eta), \tag{30}$$

where, in, addition,

$$F(k,-\beta,2f) \equiv 0. \tag{31}$$

The set of curves parametrized by this constraint will intersect the curves defined by Eq. (29) at certain isolated *points* in the β-k plane. By finding these intersection points, we determine the quantized values of β and k corresponding to solutions of Eq. (23) which satisfy the boundary conditions. It is not clear at this stage of the discussion how many intersections there are, or even how the curves defined by each equation separately will look. Before we analyze the different branches of these equations and identify their intersections based on asymptotic methods in Sec. IV, it is useful to discuss in more detail the consistency of the fields thus obtained.

D. Behavior at the focal point

The main experimental purpose of the cavity is to concentrate the field near the focus as much as possible. Since one always has $E_z = 0$ there, it remains to discuss the behavior of $E_\pm$ in the focal region. Because of the "angular momentum barrier" on the right-hand side of Eq. (23), the solutions F given in Eq. (27) attain a factor $\xi^{n/2}$, which suppresses the field near the origin $\xi = 0$ when $n \neq 0$. The Kummer function itself goes to $M = 1$ at $\xi = 0$, so that the only way of obtaining a nonvanishing field at the origin is to set $n = 0$ in Eq. (26). This means that the angular momentum quantum number must in fact satisfy $m = 1$ for E_- or $m = -1$ for E_+ according to Eq. (24). However this leads to a contradiction: if the field is nonzero at the origin, then because of the azimuthal factor $\exp(\pm i\phi)$ one faces a singularity at $\xi = \eta = 0$ in which the field is indeterminate. Therefore, there is *no possibility* of obtaining a nonzero field precisely at the focus of the cavity.

For $m = \pm 1$ there are still solutions of Eq. (23), but they must involve solutions of Eq. (23) in suitable linear combinations such as to yield a vanishing field at $\xi = \eta = 0$. We have the freedom to combine eigenstates of the wave equation linearly at the same wave number k (yielding a stationary state with monochromatic time dependence). First we use the real-valued solutions in Eq. (27) to form a superposition of the type Eq. (30) with a plus sign. Despite its symmetry it

can also be made to vanish at $\xi = \eta = 0$, if one or both of the functions $F(k,\beta,\xi)$ and $F(k,-\beta,\eta)$ are zero at the origin.

However although we can find solutions for arbitrary m with a tangential electric field that is symmetric under reflection at the focal plane, we can only attempt to concentrate the field *near* the focus, always with a node at the focal point, dictated for $m \neq 0$ by the phase singularity at the origin. For $m = 0$, there is the residual angular momentum barrier due to $n \neq 0$, and thus even in this simple case—contrary to our expectation from quantum mechanical analog—the "s-wave" solutions have a vanishing field at the focus, as a consequence of the vector nature of the field.

E. Particular case: fundamental s wave

The case $m = 0$ can be discussed in more detail because it permits simple analytical expressions for the wave solution, if we specialize further to $\beta = 0$. In this case, the solutions in Eq. (27) simplify to

$$F(k,0,\xi) \propto I\left(\frac{n}{2}, \frac{i}{2}k\xi\right) i^{n/2}, \tag{32}$$

dropping prefactors that are absorbed in the normalization. Here I is the modified Bessel function.

As was already noted below Eq. (15), $E_\pm$ is linearly dependent in the special case $m = 0$, so that we can in particular choose $E_+ = E_-$. Then $E_\rho = 0$ and $E_+ = E_- = E_\phi/\sqrt{2}$. We thus obtain the TE field by setting

$$E_\phi = Q = F(k,0,\xi)F(k,0,\eta), \tag{33}$$

as in Eq. (25). This already satisfies the condition of symmetry with respect to the focal plane, without having to form a superposition of the type of Eq. (30). Moreover, it satisfies the condition of vanishing divergence, as can be checked with Eq. (17).

With $n = 1$ (for E_+ at $m = 0$), Eq. (32) can be rewritten to obtain

$$\vec{E} = \begin{cases} E_\xi = 0 \\ E_\eta = 0 \\ E_\phi = E_0 \dfrac{1}{k\sqrt{\xi\eta}} \sin(k\xi/2)\sin(k\eta/2) \end{cases} \tag{34}$$

and

$$\vec{B} = \begin{cases} B_\xi = -iE_0 \dfrac{\sqrt{\mu\epsilon}}{k} \sqrt{\dfrac{1}{\xi+\eta}} \dfrac{1}{\sqrt{\xi}} \sin(k\xi/2)\cos(k\eta/2) \\ B_\eta = +iE_0 \dfrac{\sqrt{\mu\epsilon}}{k} \sqrt{\dfrac{1}{\xi+\eta}} \dfrac{1}{\sqrt{\eta}} \cos(k\xi/2)\sin(k\eta/2) \\ B_\phi = 0. \end{cases} \tag{35}$$

The resonance condition is obtained from the boundary condition [Eq. (6)] on the parabolic dome at $\xi = 2f$ as

$$k_N = N\frac{\pi}{f}, \quad N = 1,2,\ldots . \tag{36}$$

A relatively simple visualization of these modes can be obtained by expressing the electric and magnetic fields in cylindrical and spherical coordinates which are more familiar. It can be verified using the relations between these coordinates to the parabolic variables that Eq. (34) then takes the form

$$\vec{E} = \begin{cases} E_\rho = 0 \\ E_z = 0 \\ E_\phi = E_0 \dfrac{1}{k\rho}(\cos(kz) - \cos(kr)), \end{cases} \quad (37)$$

and the corresponding magnetic field is

$$\vec{B} = \begin{cases} B_\rho = iE_0 \dfrac{\sqrt{\mu\epsilon}}{k} \dfrac{1}{r\rho}(z\sin(kr) - r\sin(kz)) \\[2mm] B_z = iE_0 \dfrac{\sqrt{\mu\epsilon}}{k} \dfrac{\sin(kr)}{r} \\[2mm] B_\phi = 0. \end{cases} \quad (38)$$

By splitting the various terms appearing here into two contributions, the electromagnetic field can then be considered as the superposition of two fields:

The first field is polarized along E_ϕ and B_ρ, and can be expressed in cylindrical coordinates as

$$E_\phi^{(1)} = \frac{E_0}{k_N\rho}\cos(k_Nz) \quad \text{and} \quad B_\rho^{(1)} = i\sqrt{\mu\epsilon}\frac{E_0}{k_N\rho}\sin(k_Nz) \quad (39)$$

The second field is polarized in spherical coordinates (r, ϕ, θ) along the directions of the azimuthal and polar angles, ϕ and θ, according to

$$E_\phi^{(2)} = \frac{E_0}{\sin\theta}\frac{\cos(k_Nr)}{k_Nr} \quad \text{and} \quad B_\theta^{(2)} = i\sqrt{\mu\epsilon}\frac{E_0}{\sin\theta}\frac{\sin(k_Nr)}{k_Nr}. \quad (40)$$

Here we have used the substitution $\rho = r\sin\theta$ in the denominators.

The first field, [Eq. (39)] corresponds to cylindrical standing waves with a phase variation along the z direction, while the second field [Eq. (40)] corresponds to spherical standing waves with a phase variation along the radial direction. This configuration is reminiscent of what is expected from a simple geometrical optics argument in which a ray bundle emerging from the focal point can propagate outward as a spherical wave. Upon reflection on the parabola it is converted into a cylindrical wave, which in turn can counterpropagate back to the focal point after being reflected on a planar mirror and a second time on a parabola. In an unfolded double paraboloid, the ray trajectories are of the type shown in Fig. 4. It should be noted that these two partial waves are not physical when taken individually, because in both cases the electric field diverges along the axis of the parabola. The divergence, however, cancels out when the superposition of the two partial waves is considered. So far we have only drawn this ray interpretation from a particular decomposition of the exact solution; the question is how arbitrary this decomposition is, and what we can learn from it.
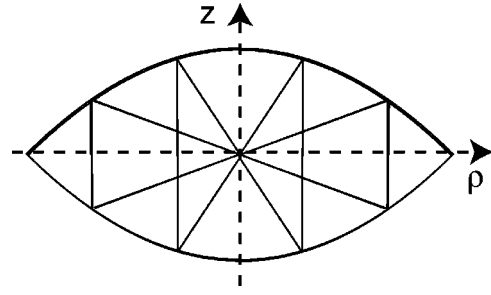

FIG. 4. Cross-sectional view of the unfolded cavity with two closed, bowtie-shaped ray paths going through the common focus of the bounding parabolas. Families of such rays can be thought of as constituents of the s wave in Eq. (34).

This will be pursued in Sec. IV. The actual intensity distribution of these $n=1$ states in the cavity will be plotted in Sec. V B, where we can compare their spatial patterns with those obtained for larger n, in order to justify our claim that s-wave modes provide the best focusing.

IV. FINDING THE MODES WITHIN THE SHORT-WAVELENGTH APPROXIMATION

Having seen that even the long-wavenlength s waves in our cavity can be interpreted as standing waves arising from counterpropagating ray bundles and their accompanying wave fronts, we now turn to a more quantitative eikonal analysis. Such an analysis can provide accurate starting points for a numerical search of the exact wave solutions, which are determined by finding intersection points between the families of curves (29) and (31) in the plane of β vs k. Such semiclassical considerations, based on the short-wavelength approximation, are an important first step because there are, as we shall see, infinitely many intesections between the sets of curves determining the exact solutions, and one desires a means of finding them in a systematic way, labeling them by ''quantum numbers,'' giving the number of nodes in the field along the coordinate lines for ξ and η. Beyond this very practical use of the short-wavelength limit, we also want to establish a physical understanding of the resonator modes that allows us to predict how they depend on changes in the cavity shape. This aspect of the ray picture will be expounded upon in Sec. VIII

A. WKB approximation and effective potential

The equation to be solved is Eq. (26), an ordinary second-order differential equation, where the angular momentum m enters as a parameter trough the constant n. We are looking for solutions $F(\xi)$ which satisfy the boundary condition $F(2f) = 0$ and are not singular at $\xi = 0$. The standard short-wavelength approach to be employed here is the WKB approximation [14]. After division by ξ, Eq. (26) takes the form

$$\frac{d^2f}{d\xi^2} + \frac{1}{\xi}\frac{df}{d\xi} + \frac{1}{4}\left(k^2 + \frac{4\beta}{\xi} - \frac{n^2}{\xi^2}\right)f(\xi) = 0. \quad (41)$$

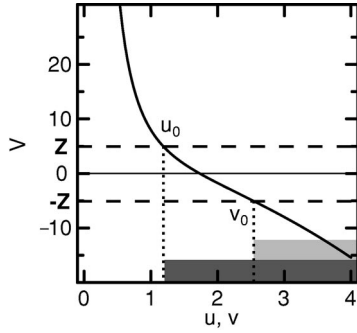For subsequent analysis it is convenient to introduce a dimensionless coordinate

FIG. 5. Solid curve: the effective potential $V(u)$ for $n=3$, showing the classical turning points u_0 (v_0) where Z ($-Z$) intersects the effective potential V (cf. the dashed lines). The ranges of classically allowed motion for the two degrees of freedom u and v with energies Z and $-Z$ are indicated by the shaded bars (dark for u, light for v). The outer turning points at $u, v = \sqrt{2kf}$ act as a hard wall whose position depends on k.

$$u = \sqrt{k}\,\xi. \tag{42}$$

Dividing Eq. (41) by k^2, and defining a rescaled separation constant

$$Z \equiv \frac{4\,\beta}{k}, \tag{43}$$

the following equation is obtained:

$$-\frac{d^2f}{du^2} - \frac{1}{u}\frac{df}{du} + \frac{1}{4}\left(\frac{n^2}{u^2} - u^2\right)f(u) = Zf(u). \tag{44}$$

This has a form similar to the one-dimensional Schrödinger equation of quantum mechanics, except for the first u-derivative which makes the kinetic energy operator non-self-adjoint. This term appears in the radial equation of cylindrically symmetric problems, but does not affect the applicability of the WKB approximation [15].

The WKB solution requires us to find the classical turning points in the potential appearing in this equation, with Z playing the role of the total energy. This effective potential

$$V(u) = \frac{1}{4}\left(\frac{n^2}{u^2} - u^2\right) \tag{45}$$

is a superposition of an inverted parabola and the centrifugal potential determined by n, giving rise to the solid line in Fig. 5. Using this together with the ansatz

$$f(u) \approx \frac{1}{p(u)}e^{i\int p(u)du}, \quad p(u) = \sqrt{Z - V(u)}, \tag{46}$$

approximate solutions are found by imposing the boundary conditions at the turning points.

There is only one possible turning point corresponding to the closest approach to the origin $u=0$, which is given by

$$V(u_0) = Z \Rightarrow u_0 = \sqrt{\sqrt{n^2 + \frac{Z^2}{4}} - \frac{Z}{2}}. \tag{47}$$

If $Z > 0$ and $n=0$, then no inner turning point exists. This inner turning point, in classical mechanics, is the point where the momentum in the x direction smoothly goes through zero as it changes sign, and hence the probability per unit time of finding the particle becomes infinite. In the ray dynamics, this phenomenon gives rise to a *caustic*. This will be discussed further in Sec. VI.

The outer turning point of this classical picture is determined by the Dirichlet boundary condition at the parabolic mirror, which in the new coordinate is located at

$$\xi_1 = 2f \Rightarrow u_1 = \sqrt{2\,kf}. \tag{48}$$

It is the boundary condition $f(u_1) = f(\sqrt{2\,kf}) = 0$ in which the short-wavelength condition is contained: we assume that at the outer boundary the wave function has the WKB form [Eq. (46)], which requires that the dimensionless *size parameter* satisfies

$$x \equiv 2\,kf \gg 1, \tag{49}$$

i.e., this additional boundary is far away from the classical turning point u_0 of the effective potential. All steps discussed above for $f(\xi)$ apply analogously to the variable η appearing in the product ansatz Q [Eq. (25)], if we reverse the sign of Z everywhere and replace u by the variable

$$v = \sqrt{k}\,\eta. \tag{50}$$

Then the inner turning point v_0 for this second degree of freedom is obtained as

$$V(v_0) = -Z \Rightarrow v_0 = \sqrt{\sqrt{n^2 + \frac{Z^2}{4}} + \frac{Z}{2}}. \tag{51}$$

The values of u_0 and v_0 determine the distance of closest approach to the z axis.

B. Quantization conditions

Under this condition, the semiclassical determination of the eigenfrequencies proceeds by applying the Bohr-Sommerfeld quantization to the action integral for one period of the motion in the effective potential. One round trip consists of the path from u_0 to u_1 and back to u_0. The quantized action is therefore

$$J(Z,x;n,\nu) \equiv 2\int_{u_0}^{u_1}\sqrt{Z - V(u)}\,du \equiv 2\pi\left(\nu + \frac{3}{4}\right). \tag{52}$$

The integer $\nu = 0,1\ldots$ is the number of nodes of the wave function in the potential, and the constant 3/4 takes into account the phase shifts of π and $\pi/2$ at the outer and inner turning points, respectively. In other words, the above quantization condition is an approximate way of writing the phase-shift requirements that hold at boundaries and caustics, using the approximation that the wave propagation itself is described by a wave front whose phase advance in x is given by the function J.

The result of the integration is found to be

$$J(Z,x;n,\nu) = \sqrt{x^2+Zx-n^2} + \frac{Z}{2}\ln\frac{\sqrt{x^2+Zx-n^2}+x+Z/2}{\sqrt{n^2+Z^2/4}}$$

$$-n\left(\arcsin\frac{Zx-2n^2}{x\sqrt{Z^2+4n^2}}+\frac{\pi}{2}\right)$$

$$=2\pi\left(\nu+\frac{3}{4}\right). \tag{53}$$

This is an equation for the two unknowns Z and x, i.e., for the rescaled separation constant and size parameter. It is therefore analogous to Eq. (29). The integer ν uniquely labels all the allowed solutions f_ν of Eq. (44). This is an important difference to Eq. (29): there, the function F in fact has infinitely many *branches* that satisfy the equation, which, however, are not labeled explicitly. The great advantage of Eq. (53) is that these branches are explicitly enumerated by ν, so that fixing this index selects exactly one curve in the Z-x plane instead of an infinte family.

As in Eq. (25), the field consists of products of the form

$$Q=f_\nu(x,Z,u)f_\mu(x,-Z,v), \tag{54}$$

with v defined as in Eq. (50). The two function f_ν and f_μ have their analog in the exact solutions F of Eq. (26), corresponding to the branches of F labeled by ν and μ, respectively.

We then form combinations the form of Eq. (30) to enforce the required symmetry with respect to the focal plane. The semiclassical WKB quantization for the function $f_\mu(x,-Z,v)$ provides a second equation of the form of Eq. (53):

$$J(-Z,x;n,\mu)=2\pi(\mu+\tfrac{3}{4}). \tag{55}$$

These two quantization conditions play the same role as Eqs. (29) and (31): the intersections of the curves parametrized by them determine the quantized values of Z and x. However, the WKB method affords a great simplification: by fixing the branches ν and μ, the intersection of the two resulting curves is uniquely determined. To illustrate this situation, in Fig. 6 we show how the lines defined by the above two equations traverse the Z-x plane. Only a small portion of this plane is shown, emphasizing the behavior of the semiclassical results at small x where their accuracy should be at a minimum. Comparison with the exact families of curves shows, however, that the WKB results are excellent even in this long-wavelength limit. Note that, by symmetry, intersections occurring at $Z=0$ are always between curves with the same branch index $\nu=\mu$. All curves shift to larger x with increasing n because of the larger centrifugal barrier, pushing the classically allowed regions of the effective potential in Fig. 5 outward.

V. EXACT SOLUTION FOR THE MODES AND THEIR FIELD DISTRIBUTION

Once the allowed combinations of Z and x—or equivalently β and k—at which the boundary conditions are satisfied have been found, the problem of finding the modes is solved. For example, we can now plot the intensity distribution of each mode by using the quantized values of β and k
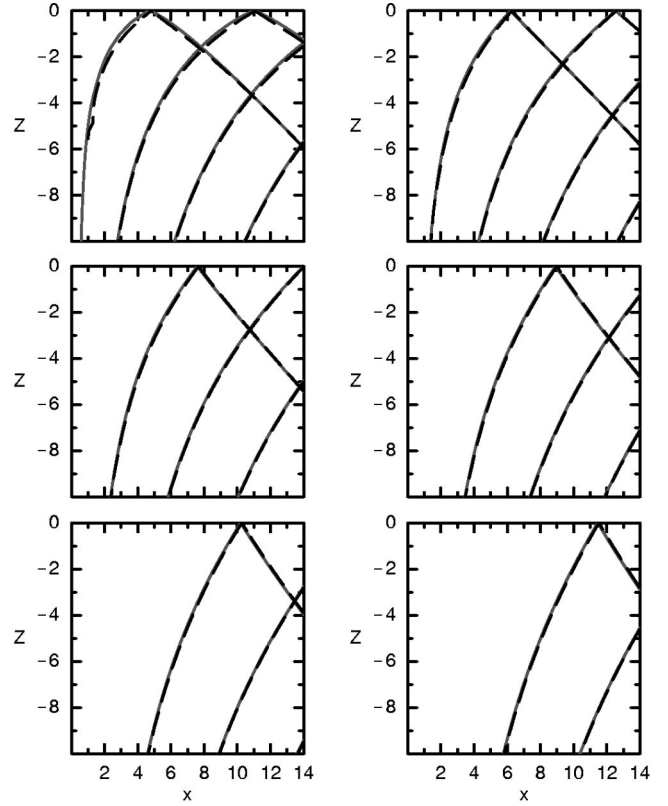

FIG. 6. For the first six values of n, the graphical solution of the simultaneous equations (53) and (55) can be read off from the intersections of the gray curves. The dashed black curves show the analogous graphical solution of Eqs. (29) and (31). The exact and semiclassical curves are almost indistinguishable (except for $n=0$), attesting to the striking accuracy of the former even at the smallest possible size parameters x. All plots can be continued to $Z>0$ by reflecting at the axis $Z=0$. The WKB curves with positive slope belong to Eq. (55), and the falling lines are created by Eq. (53). They are labeled starting from the leftmost by $\mu,\nu=0,1,2\ldots$.

in Eq. (27), and forming the proper linear combinations of the form of Eq. (30).

A. Mode profiles

This will now be carried out for the lowest-lying modes as obtained from the intersections in Fig. 6. Any given value of n can have a different meaning for the intensity distribution in the azimuthal direction, depending on which case in Eq. (24) we choose to consider: $n=m\pm1$ for the modes. Since the azimuthal field variation is trivial, $\propto\exp(im\phi)$, we wish to restrict our attention to the mode profile in the plane spanned by ρ and z in cylindrical coordinates. The variable governing this property is n, not m. Therefore, n is used here to classify the mode profiles.

As in the previous sections, we shall take the focal plane to be the symmetry plane of a double paraboloid, and plot the wave fields in this unfolded cavity. This is done in view of the subsequent discussion, where we shall establish the connection between these modes and the ray dynamics. Some wave plots are shown in Figs. 7 and 8. Note that the case $n=0$ does not appear among the solutions listed here because it corresponds to wave fields that do not vanish on
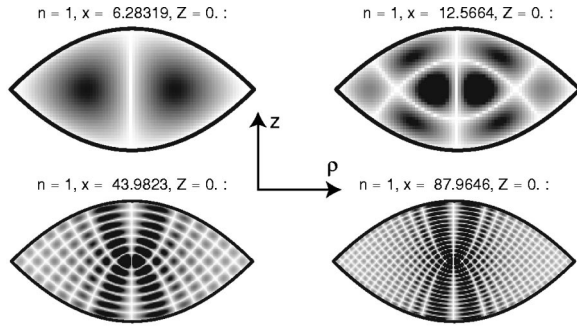
FIG. 7. Four states with $n=1$. The grayscale indicates the magnitude of the electric field for the modes ($E_\pm$) of the confocal double paraboloid, and the highest fields are shown in black. The vertical axis is z, and the horizontal axis is the axial distance ρ. Increasing x means a shorter wavelength and hence more nodal lines (white). The size parameter is quantized according to Eq. (56), with $N=1$ and 2 in the top row, and $N=7$ and 14 at the bottom.

the z axis and hence are irreconcilable with the finite angular momentum $m=\pm 1$, as discussed in Sec. III D).

If we look at only the left column of Figs. 7 and 8, it is apparent that all states with $Z=0$ look similar, as do all states with $Z\neq 0$. A similar observation can be made in the right columns of the figures. Comparison to the intersecting lines in the graphical solution, Fig. 6, shows that states with the same nodal pattern indeed result from the crossing of the same pair of lines—labeled by the same μ and ν, only for different n which pushes the intersecting lines to higher x.
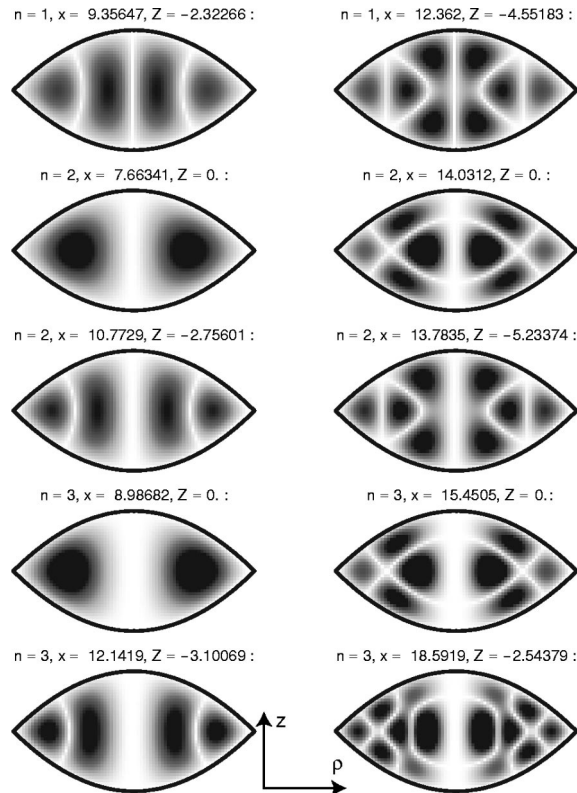

FIG. 8. The modes shown here do not follow the simple law of Eq. (56), but were obtained numerically. With increasing centrifugal barrier, labeled by n, the forbidden region around the z axis grows outward.

However, the interpretation of μ and ν as the number of nodes in the parabolic coordinate directions cannot be carried through in all of the plots. We will return to this problem in Sec. V C.

In order to achieve the best possible concentration of fields near the focus, the most promising candidates are modes with $n=1$. Among these, the patterns shown in Fig. 7 indicate that the states at $Z=0$ in turn show the highest intensity near the focal plane. These are precisely the fundamental s waves we discussed in Sec. III E, with the wavenumbers quantized according to Eq. (36), which for the size parameter reads

$$x_N = 2\,k_n f = 2\,\pi N. \tag{56}$$

This is an exact result which can be compared to the WKB quantization condition in Eq. (53), with $Z=0$ and $n=1$. The latter actually has a more complicated form,

$$\sqrt{x^2-1} + \arcsin\frac{1}{x} = 2\,\pi(\nu+1), \tag{57}$$

but to second order in the small quantity $1/x$ this is identical to Eq. (56) with $N=\nu+1$. This confirms the observation made in Fig. 6 that the numerical agreement between exact and semiclassical solutions is good even for small quantum numbers.

B. Focussing and the effective mode volume

In order to evaluate the field enhancement that is achieved in the fundamental TE modes discussed in Sec. III E and shown in Fig. 7, it is necessary to examine the distribution of the electromagnetic energy in that mode. The energy in a parabolic cavity of focal length f is

$$U = \frac{1}{4}\int_{\xi=0}^{\xi=2f}\int_{\eta=0}^{\eta=2f}\int_{\phi=0}^{\phi=2\pi}\left(\frac{\epsilon}{2}(|E_\xi|^2+|E_\eta|^2+|E_\phi|^2)\right.$$
$$\left.+\frac{1}{2\mu}(|B_\xi|^2+|B_\eta|^2+|B_\phi|^2)\right)\frac{\xi+\eta}{4}d\xi\,d\eta\,d\phi, \tag{58}$$

which for the fundamental (s-wave) TE modes [Eq. (34)] gives

$$U = \epsilon E_0^2\frac{\pi f}{4k^2}\int_0^{kf}\frac{\sin^2(x)}{x}dx, \tag{59}$$

where the value of the integral can be evaluated numerically.

For the experimentally realized cavity described in Sec. I $kf=14\,\pi$, so that the value of the integral is 2.527. The intensity distribution for this mode is shown at the bottom right of Fig. 7 (note $x=2\,kf$). To examine the energy distribution in the cavity, we can evaluate the energy that is contained at each lobe of the standing wave of parabolic wave front that corresponds to the mode. We note then that the first lobe, corresponding to a parabolic wave front of focal length $f_1=\lambda/2$, contains 48% of the total energy; to see this, replace the integration limit in Eq. (59) by π. This lobe

occupies a physical volume of $V_0 \equiv \pi \lambda^3/4$, whereas the volume of the overall cavity, $V = 2\pi f^3$, is 2744 times larger.

This underscores the very large confinement of the field that occurs in the vicinity of the focal point, and points to the possibility of observing a very large enhancement of spontaneous emission into this mode. The fraction of the total energy contained in the first lobe of course reaches 100% if the smallest possible cavity with $kf = \pi$ is considered. However, the size achieved in our present sample already approaches the optimal conditions if one takes into account that enhancement of spontaneous emission requires not only a small effective mode volume but most of all a small local density of states [16]. The *average* density of modes in an arbitrarily shaped electromagnetic resonator of volume V is a fundamental quantity in the theory of blackbody radiation and was derived by Weyl [17]:

$$\rho_{\text{Weyl}}(k) \approx \frac{k^2}{\pi^2} V. \tag{60}$$

Note that this can also be written in the physically intuitive form

$$\rho_{\text{Weyl}}(k) \approx \frac{2}{3}\pi^2 \frac{d}{dk}\left(\frac{V}{V_0}\right), \tag{61}$$

indicating that the number of modes in the interval dk is proportional to the number of additional volume quanta V_0 that fit into the given volume V when k increases to $k + dk$. The *local* density of states in the focal volume V_0 can therefore be interpreted to be the same as the total density of states in a small cavity of volume $V = V_0$. This, in turn, is roughly the effective mode volume for the fundamental *s* wave in our structure. From this we conclude that the spontaneous emission enhancement should be close to the maximum possible value even though our cavity is not of the minimum possible size. This is one of the central advantages we were looking for in the parabolic cavity design. In this discussion we have assumed for simplicity that the Q factor of the modes under consideration is fixed, independent of size and quantum numbers. This severe simplification will be removed in Sec. VIII.

In higher order modes with $m > 0$, the centrifugal barrier prevents the field from approaching the focal point. This implies that these modes will have a larger effective volume and, correspondingly, a smaller enhancement of the spontaneous emission rate. An added difficulty concerning the higher order modes arises from the limited experimental control over the exact cavity shape. As discussed in Sec. VII, small deformations of the cavity (modeled as deviations from confocality) result in chaos, leading to a loss of constraints on the possible regions of phase space which can be explored. This further increases the effective volume of these modes. The enhanced spontaneous emission into the fundamental *s* wave implies that this mode will also exhibit a large gain and, correspondingly, a low lasing threshold. The preliminary conclusion of this section is therefore that a mode with low angular momentum and small Z (or β) will be the dominant mode in a laser of parabolic geometry.
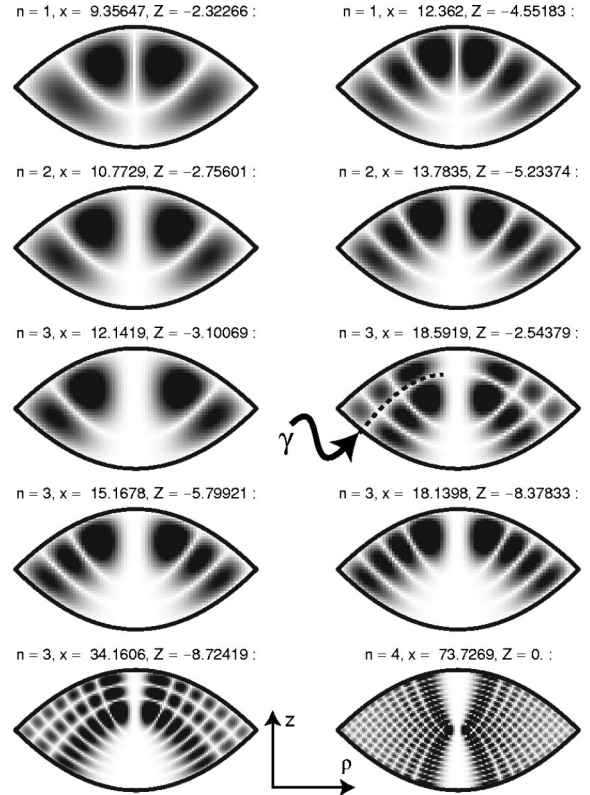

FIG. 9. Mode intensities as in Fig. 8, but without performing the symmetrization prescribed by the focal plane boundary condition. The WKB quantum numbers μ (and ν) can be read off by counting the number of wave function nodes parallel (and perpendicular) to the reference line γ. Modes in the first three rows correspond to the symmetrized versions of Fig. 8. In order to illustrate the approach to the short-wavelength limit, additional modes are shown for which the formation of caustics is apparent in the high-intensity ridges (black) bordering the classically forbidden regions (white).

C. Caustic structure in the wave solutions

In order to arrive at the solutions shown in Fig. 8, we started from the semiclassical (short-wavelength) approximation and then refined the quantized Z and k further by applying the exact modal conditions. However, the question arises how the quantum numbers μ and ν which label the semiclassical solutions can be visualized in Fig. 8. The answer is that the symmetrization procedure obscures this identification. What happens can be understood if we ignore the parity requirement and plot the wave fields in the simple product form of Eq. (25).

The symmetrization performed according to Eq. (30), with $A = B$, introduces no change whatsoever if the separation constant is $\beta = 0$. Therefore, the intensity profiles of all modes with $Z = 0$ in Fig. 8 are the same before and after symmetrization. However, the wave patterns acquire a qualitatively different and simpler form if we desymmetrize the remaining states. This is shown in Fig. 9. The nodal patterns now appear in a regular fashion along the coordinate lines for u and v (or ξ and η), and their number along these lines is uniquely determined by μ and ν.

By symmetrizing a state such as the one shown for $n = 3$, $k = 18.59$, and $Z = -2.54$ in Fig. 9, the field shown in the desymmetrized plot is added to its reflection at the focal

plane, thus allowing some nodal lines to be ''filled in,'' as seen in the corresponding state at the bottom right of Fig. 8. The desymmetrized waves in Fig. 9 exhibit nodal lines precisely along lines of $\eta = $ const or $\xi = $ const. In addition to the simple nodal structure, we also observe a clear segregation between regions of negligible intensity and regions of oscillatory field, with dividing lines between them that become more and more pronounced as the size parameter $x = 2kf$ increases. These are the caustics, which in fact accumulate an increasing amount of intensity as the short-wavelength limit is approached. The caustics follow parabolic coordinate lines as well, as is apparent from the last row of Fig. 9. The field at $n=3$, $x=34.16$, and $Z=-8.72$ is bounded from below by a broad inverted parabola, and excluded from the z axis by a steep upright parabola. The intersection of both parabolas forms the caustic. In the mode at $n=4$, $x=73.73$, and $Z=0$, both the upright and inverted bounding parabolas are symmetric as we expect for $Z=0$.

VI. CAUSTIC STRUCTURE IN THE RAY PICTURE

In this section we will elaborate on the relation between mode structure and ray dynamics, as a basis on which we can predict the effect of shape perturbations on the mode structure. The caustic patterns revealed in Sec. V, by the decomposition into the product states as in Eq. (25), are a direct consequence of the classical turning points in the effective potential V, [Eq. (45)], for the motion along the ξ and η directions. The distinction between classically allowed and forbidden regions gives rise to the regions of oscillatory and vanishing fields in Fig. 9. The effective potential has, so far, been discussed only as an auxiliary concept that proved convenient in the WKB treatment; its relation to the behavior of the rays of geometric optics is, however, well known. For the sake of a self-contained presentation, here we convey the idea behind the general eikonal theory by showing how to derive ray equations from the one-dimensional separated wave equations, [Eq. (26)]. The argument is nonstandard in the sense that Eq. (26) is based on the full vectorial wave equation (i.e., with polarization), and we therefore shall find that for a given angular momentum m, slightly different ray trajectories have to be considered depending on polarization. This is because the quantity entering Eq. (26) is n, not m.

A. Ray equations from the WKB approximation

Inserting the WKB ansatz, [Eq. (46)] into the wave equation for the separated variables [Eq. (26)], one finds to leading semiclassical order that p must satisfy the equation

$$p_u^2 + V(u) = Z \quad \text{or} \quad \text{(similarly)} \quad p_v^2 + V(v) = -Z. \quad (62)$$

We can interpret this as the Hamiltonians of two decoupled linear systems, and add them to obtain the Hamiltonian for the combined system:

$$\tilde{H} = p_u^2 + p_v^2 + V(u) + V(v). \quad (63)$$

The trajectories we are looking for then satisfy the equation $\tilde{H}(p_u, p_v, u, v) = Z - Z = 0$, or written out:

$$p_u^2 + p_v^2 + \frac{1}{4}\left(\frac{n^2}{u^2} + \frac{n^2}{v^2} - u^2 - v^2\right) = 0. \quad (64)$$

If we divide this by $(u^2 + v^2)$, the result is

$$\frac{p_u^2 + p_v^2}{u^2 + v^2} + \frac{1}{4}\left(\frac{n^2}{u^2 v^2} - 1\right) = 0; \quad (65)$$

this can also be interpreted as arising from a *new* Hamiltonian

$$H \equiv \frac{p_u^2 + p_v^2}{u^2 + v^2} + \frac{1}{4}\frac{n^2}{u^2 v^2}, \quad (66)$$

by requiring

$$H(p_u, p_v, u, v) = \tfrac{1}{4}. \quad (67)$$

The Hamiltonian in this form is analogous to the wave equation in parabolic coordinates [Eq. (23)], where the Laplacian is divided by the same scale factor $(u^2 + v^2)$ that accompanies the conjugate momenta here. One can now use Hamilton's equation of motion to replace momenta by ''velocities,'' the definition being

$$\dot{u} = \frac{\partial H}{\partial p_u}, \quad \dot{v} = \frac{\partial H}{\partial p_v}. \quad (68)$$

This leads to the substitution

$$p_u = \tfrac{1}{2}(u^2 + v^2)\dot{u}, \quad p_v = \tfrac{1}{2}(u^2 + v^2)\dot{v}, \quad (69)$$

which brings Eq. (67) into the form

$$(u^2 + v^2)(\dot{u}^2 + \dot{v}^2) + \frac{n^2}{u^2 v^2} = 1. \quad (70)$$

Reverting to cylinder coordinates, the above equation becomes

$$k^2(\dot{\rho}^2 + \dot{z}^2) + \frac{n^2}{k^2 \rho} = 1. \quad (71)$$

Here we used the definitions of the coordinates in Eqs. (3) and (42). To examine what this equation has to do with the ray dynamics, we now take the ray-picture point of view.

B. Geometric optics in cylindrical coordinates

If we consider the three-dimensional motion of rays in a double paraboloid of the shape in Fig. 3(b), their propagation between reflections at the parabolic walls will of course follow straight lines, and hence there is no place for any coordinate-dependent potential V. However, in order to compare the ray dynamics to wave function plots in the z-ρ plane, as shown in Fig. 9, we must project the ray motion onto this plane as well. In the wave analysis, this projection was achieved by using the *rotational symmetry* of the cavity around the z axis to eliminate the azimuthal coordinate ϕ from the problem in favor of the angular momentum quantum number m.

In ray optics, we can do the same: rays can be classified by an angular momentum L_z because of the axial symmetry. To see this, we first define L_z. A ray trajectory is a curve consisting of straight line segments between each reflection. If we parametrize this curve as $\mathbf{r}(l)$, where l is the path length along the ray from some arbitrary starting point, then $|\dot{\mathbf{r}}(l)| = 1$. Here and in the following, the dot represents the differentiation with respect to arc length, d/dl. In cylinder coordinates ρ, ϕ, and z, we can decompose this as

$$\dot{\mathbf{r}} = \dot{\rho}\,\mathbf{e}_\rho + \dot{z}\,\mathbf{e}_z + r\,\dot{\phi}\,\mathbf{e}_\phi. \tag{72}$$

Between any two reflections, this is a constant unit vector in the direction of the ray. With this, the equation for a straight line segment can be written, in general, as

$$\mathbf{r} \times \dot{\mathbf{r}} \equiv \mathbf{L}, \tag{73}$$

where $\mathbf{L}$ is a constant analogous to the angular momentum of classical mechanics.

Because of the rotational symmetry around the z axis, the azimuthal unit vector $\mathbf{e}_\phi$ at the point of reflection is always tangent to the surface. Therefore, a reflection does not change the component of $\dot{\mathbf{r}}$ along $\mathbf{e}_\phi$, so that $\rho\dot{\phi}$ is continuous. Since the ray curve is itself continuous everywhere, so is $\rho(l)$. Hence the quantity

$$L_z \equiv \rho^2 \dot{\phi} \tag{74}$$

is also continuous at each reflection. But this is just the z component of $\mathbf{L}$ in Eq. (73), as can be verified by performing the cross product there. Thus L_z is a constant between reflections, which together with its overall continuity implies that it is a conserved quantity for the whole ray trajectory.

Using Eq. (74), the fact that $\dot{\mathbf{r}}$ is a unit vector [Eq. (72)], can be recast as

$$\dot{\rho}^2 + \dot{z}^2 + \frac{L_z^2}{\rho^2} = 1. \tag{75}$$

From the ray approach we have thus obtained an equation almost identical to Eq. (71). We only have to redefine the path length variable l to make it dimensionless, by introducing

$$s = k\,l, \tag{76}$$

to obtain

$$\frac{d\rho}{dl} = k\frac{d\rho}{ds}, \tag{77}$$

for the derivatives, and furthermore interpret

$$L_z = \frac{n}{k}. \tag{78}$$

Then Eqs. (71) and (75) become identical, if we interpret the dot in Eq. (71) to mean d/ds. The scale factor of the ''time'' variable parametrizing our trajectories is irrelevant for the shape of the paths, so that we can conclude that *the ray picture introduced here is equivalent to the motion described by the WKB effective potential, with the important identification of Eq. (78).*

Besides Eq. (75), the only other equation that is needed to completely determine any ray trajectory from its initial conditions is the law of specular reflection, which can be formulated with the help of the outward normal unit vector $\mathbf{u}$ at the reflection point as

$$\dot{\mathbf{r}}_{reflected} = \dot{\mathbf{r}} - 2\,\mathbf{u}(\mathbf{u}\cdot\dot{\mathbf{r}}). \tag{79}$$

This corresponds to a reversal of the normal component of $\dot{\mathbf{r}}$. Here we can see explicitly that reflections do not affect the component of $\dot{\mathbf{r}}$ in the direction of $\mathbf{e}_\phi$, since the normal $\mathbf{u}$ has no $\mathbf{e}_\phi$ component as a consequence of the axial symmetry.

This latter fact also means that we can simply drop the $\mathbf{e}_\phi$ component from Eq. (79) altogether. Therefore, we now define the two-component vectors in the z-ρ plane by dropping the $\mathbf{e}_\phi$ components from the corresponding three-component vectors. Thus $\dot{\mathbf{r}}$ becomes

$$\mathbf{v} \equiv \dot{\rho}\,\mathbf{e}_\rho + \dot{z}\,\mathbf{e}_z \equiv \begin{pmatrix} \dot{\rho} \\ \dot{z} \end{pmatrix}, \tag{80}$$

and, similarly,

$$\mathbf{u} = u_\rho\,\mathbf{e}_\rho + u_z\,\mathbf{e}_z. \tag{81}$$

In this two-dimensional space, the specular-reflection condition retains the form of Eq. (79):

$$\mathbf{v}_{reflected} = \mathbf{v} - 2\,\mathbf{u}(\mathbf{u}\cdot\mathbf{v}). \tag{82}$$

This is the reason why we can call the motion in the z-ρ plane a *billiard problem*.

C. Curved ray paths in the centrifugal billiard

We know that the trajectories between reflections are straight lines, so that the components of $\dot{\mathbf{r}}$ in the Cartesian coordinate frame are constant for each segment. In our new z-ρ frame of reference, the z axis is the same as the Cartesian one, so that we still have $v_z = \dot{z} = \text{const}$ between reflections in Eq. (80). However, the same does *not* hold for the ρ component of $\mathbf{v}$. Instead, from Eq. (75) we obtain from

$$\dot{\rho}^2 + \frac{L_z^2}{\rho^2} = 1 - \dot{z}^2 = \text{const.} \tag{83}$$

If we multiply this by $4\rho^2$, it can be written as a differential equation for ρ^2:

$$\left(\frac{d}{dl}\rho^2\right)^2 = 4\rho^2\dot{\rho}^2 = 4(1-\dot{z}^2)\rho^2 - 4L_z^2. \tag{84}$$

The solution is that $\rho^2(l)$ describes a shifted parabola,

$$\rho^2(l) = \rho_0^2 + 2(l-l_i)\sqrt{(1-\dot{z}^2)\rho_i^2 - L_z^2} + (l-l_i)^2(1-\dot{z}^2), \tag{85}$$
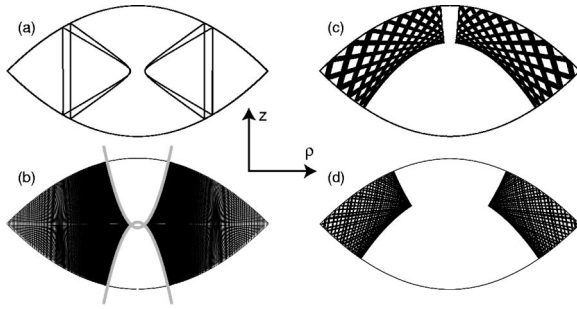
FIG. 10. All starting conditions for the rays in (a), (b), and (c) amount to the same angular momentum $L_z = 0.1f$, but prescribe different angles of incidence with respect to the boundary, and different positions of impact. (a) shows two different orbits in the same plot; both are periodic and symmetric in this projection onto the z-ρ plane, differing only in their starting points. (b) shows a single path, which is quasiperiodic because it does not close on itself even in this projection. Instead, it densely fills a region of space delimited by a caustic whose shape is given by the parabolas (gray). The caustic becomes more asymmetric in (c) and (d), each of which shows a quasiperiodic orbit. The angular momentum in (d) is $L_z = 0.6f$, leading to a larger forbidden zone around the z axis.

where ρ_i^2 is the integration constant and specifies the value of $\rho^2(l_i)$ at the starting point l_i of the ray. Since, furthermore, z is a linear function of l ($\dot{z} = \text{const}$), for definiteness we can fix the initial point is to lie on the focal plane, and substitute

$$l = l(z) = z/\dot{z} \qquad (86)$$

to find that Eq. (85) describes a curved path $\rho(z)$ in the z-ρ plane. The curved nature of this trajectory is a direct consequence of the centrifugal potential L_z^2/ρ^2 in Eq. (75), and we would recover straight lines, i.e., a linear variation of $\rho(l)$, for $L_z = 0$. This is why we refer to this problem as a *centrifugal billiard* [18]. For a visual example of how curved traces arise from stright-line trajectories, the reader is referred to Fig. 13(e), which will be discussed in Sec. VII.

An example of the ray motion in the special case $L_z = 0$ is already displayed in Fig. 4, showing no curved trajectories because there the z-ρ plane is indistinguishable from the Cartesian z-x plane. For $L_z \neq 0$, curved ray trajectories in the z-ρ plane are shown in Fig. 10 for four different initial conditions under which the ray is launched. Note that the parameter L_z, as given in the plot, has dimensions of length [cf. Eq. (75)]. This reduced two-dimensional problem can be analyzed completely without reference to the original three-dimensional ray tracing, with L_z as a parameter that encapsulates the third degree of freedom ϕ which has been eliminated. We have, broadly speaking, converted to a corotating frame of reference (with rotation speed always matching the varying angular velocity of the ray), and thus obtained a planar problem in which we now look for the classical orbits. The simplification is considerable because the three-dimensional ray motion in the cavity is rather difficult to visualize, compared to the motion in the z-ρ plane.

The two periodic orbits in Fig. 10(a) exemplify this situation: after the trajectory completes one round trip in the z-ρ plane, it returns to its initial position with the initial orientation—but in the original three-dimensional cavity

there has also been a motion in ϕ which does not necessarily amount to a full rotation around the z axis. Hence this periodic orbit of the centrifugal billiard is not in general a true periodic orbit of the parabolic dome [cf. Fig. 13(e)]. However, we can reverse this statement and conclude that any periodic orbit of the three-dimensional problem must also be periodic in the z-ρ plane. This cautionary remark concerning the interpretation of Fig. 10 is relevant if we attempt to interpret the actual modes of the original cavity in terms of a naive physical optics approach: one might think that a quantized mode has to be associated with ray paths that form a closed loop, and in this way ''reproduce'' themselves. However, a comparison between Figs. 9 and 10 reveals that periodic orbits seem to play no special role for the mode structure.

What shapes the modes is not any single periodic ray orbit, but the caustics as they appear in Fig. 10(b)–10(d). The spatial distribution of the ray trajectories exhibits a clear correspondence with the modal intensities shown in Fig. 9, particularly in the shape of the caustics. This is most convincing for the two examples in the bottom row of Fig. 9, where the wavelength is shortest: The state at $n = 3$, $x = 34.16$, and $Z = -8.72$ should be compared to Fig. 10(c), and the reflection-symmetric mode with $n = 4$, $x = 73.73$, and $Z = 0$ finds its counterpart in Fig. 10(d).

Caustics are immediately generated when we follow a single quasiperiodic orbit, but not so for a periodic one. However, periodic orbits occur in infinite families which, when plotted together, again fill a region of space bounded by a caustic curve. The two members of the family shown in Fig. 10(a) are obtained by launching a ray from the focal plane, perpendicular to it, differing only in the radial distance ρ of the launch. All other siblings of the examples in Fig. 10(a), combined, would create a picture almost identical to the one generated by the single quasiperiodic orbit in Fig. 10(b)—the latter is in fact the result of only a slight deviation from the initial conditions chosen in Fig. 10(a), with the result that the orbit *almost*, but not quite, closes in on itself after one round trip, and continues to fall short of closing itself after each subsequent round trip as well. The conclusion is that from the point of view of the caustic structure in our system, there is no qualitative difference between periodic and quasiperiodic orbits.

The fact that all orbits can be characterized by a particular caustic which they touch, and that moreover all periodic orbits come in infinite families, is a general property of *integrable* Hamiltonian systems, to which the special centrifugal billiard defined here belongs. That the paraboloid billiard is integrable, can already be concluded from the existence of a separation ansatz for the wave equation, which we discussed in Sec. III. However, we have not yet completed our program of connecting the ray and wave approaches, and in particular have not addressed the question of how to determine quantitatively the type of ray trajectories that correspond to a given mode. So far, the correspondence was established by visual inspection alone. The quantitative connection is obtained by comparing the ray patterns of Fig. 10 with the effective potential V of Eq. (45). We shall see that, for an integrable system, we can in fact uniquely connect a particular caustic with a given mode.

As a final remark concerning the periodic orbits in this integrable system, it is worth comparing the patterns of Fig. 10(a) and especially Fig. 4 with the ''bowtie laser'' of Ref. [19]. There, a semiconductor cavity was designed in such a way as to obtain lasing from a bowtie-shaped mode with highly desirable properties, foremost among them its focusing action in the center of the cavity. The focusing patterns of Fig. 4 are very similar, but the main difference is that in our case these orbits occur in families whose members can cross the $z=0$ plane with all possible axial displacements ρ. In the semiconductor cavity, most rays move on chaotic trajectories, and only a small range of initial conditions for the rays lead to a stable bowtie pattern, leading to modes which are strongly concentrated near a unique bowtie path, and hence even less spread out in space than the examples shown in Fig. 7. This leads us to anticipate that the beneficial properties of the $n=1$ modes found for our integrable system can in fact be enhanced if we allow for the possibility of chaos in the ray dynamics.

D. Connection with the effective potential in parabolic coordinates

The classical turning points for the two degrees of freedom u and v in the potential of Eq. (45) determine the parabolas which describe the caustics in Fig. 10. We note that the caustics (and also the quasiperiodic rays that generate the caustics we show) have a well-defined distance of closest approach ρ_0 with respect to the z axis, given by the corner at which the two bounding parabolas meet. Describing this in parabolic coordinates, we find that ρ_0 is approached if both ξ and η simultaneously reach their inner turning points. Expressing this condition in terms of Eqs. (47) and (51), we obtain the simple *semiclassical* relation

$$\rho_0 = \frac{n}{k}. \tag{87}$$

Here we have used the coordinate transformation $\rho = \sqrt{\xi \eta}$ [cf. Eq. (3)], and the definition of the rescaled variables [Eq. (42)].

The distance of closest approach for individual *periodic* orbits is not given by this expression, but the minimal ρ over the whole *family* of such orbits does follow this law. The caustics in Figs. 10(b)–10(d) exhibit cusp singularities at ρ_0 because, in that extreme point, the z motion has zero velocity: it is clear from Eq. (75) that the smallest ρ will be achieved when $\dot{\rho} = \dot{z} = 0$. But from the same equation we immediately obtain that the angular momentum then equals the axial distance, and with Eq. (87) this reproduces Eq. (78). We have therefore established that the ray's ''angular momentum'' is directly proportional to the modified angular momentum quantum number n of the mode under consideration. In the semiclassical limit of large k, the difference between $n = m \pm 1$, and m becomes negligible in this expression, so that we recover the intuitively expected proportionality

$$L_z = \rho_0 \approx \frac{m}{k}. \tag{88}$$

This approximation means that we can neglect the effect of polarization on the ray-wave correspondence in the semiclassical limit—however, we shall make use of this only later, in the ray analysis of Sec. VII. Since we have been interested in states at rather small k and in particular $n \geqslant 1$, in Fig. 10 we plot only trajectories with $L_z \neq 0$.

A second semiclassical relation follows from Eqs. (47) and (51) if we ask for the value z_0 of z corresponding to the point u_0, v_0 at which the caustics have their singularities. The whole caustic is uniquely determined by its singular point at radial distance ρ_0 and height z_0, cf. Fig. 10. According to Eq. (3), we obtain

$$z_0 = \frac{Z}{2k}. \tag{89}$$

This identifies the meaning of the separation constant Z, also quantifying the earlier observation that for $E=0$ both the wave and ray patterns are symmetric with respect to the focal plane: in this case, the cusp occurs on this mirror plane, as in Fig. 10(b).

With Eqs. (78) and (89), we have completed the bridge from the exact wave equation via semiclassical WKB quantization to the ray caustics. By specifying the quantized n, Z, and k of a given mode, we uniquely determine a caustic, and with it a particular family of ray paths. Now we can use additional properties of the ray picture to better understand the cavity modes. This is especially promising in this system because we have seen that the semiclassical approximation is extremely accurate here. The reason for this somewhat surprising accuracy lies itself in the properties of the ray dynamics, but in order to make this clearer we need to introduce the concept of a phase space in which the ray dynamics can be described.

E. Families of rays and Poincaré sections

A phase-space description is often used in classical mechanics because it carries more information about the possible trajectories than mere real-space diagrams. This approach was recently applied to the analysis of ray dynamics in optical cavities as well [20,21], with the goal of providing insights that are not revealed by ray tracing in real space. In particular for the treatment of non-integrable resonator geometries, it has proved valuable to represent the phase space of the rays in terms of Poincaré surfaces of section (SOS). For our purposes, the following SOS will be chosen:

It is easy to convince ourselves by recalling Fig. 3 that any ray trajectory in the cavity has to encounter the focal plane infinitely many times as it propagates. However, the radial distance of these crossings, as well as the value of $\dot{\rho}$ may vary from one crossing of this plane to the next. Now we can consider

$$\rho \quad \text{and} \quad p_\rho \equiv \dot{\rho} \tag{90}$$

as a pair of canonically conjugate position and momentum variables, and attempt to image the subset of phase space spanned by them. In order to do this, we launch a ray trajectory and follow it for many crossings of $z=0$, each time recording the instantaneous values of ρ, p_ρ as a point in a two-dimensional graph. The result is shown in Fig. 11. A
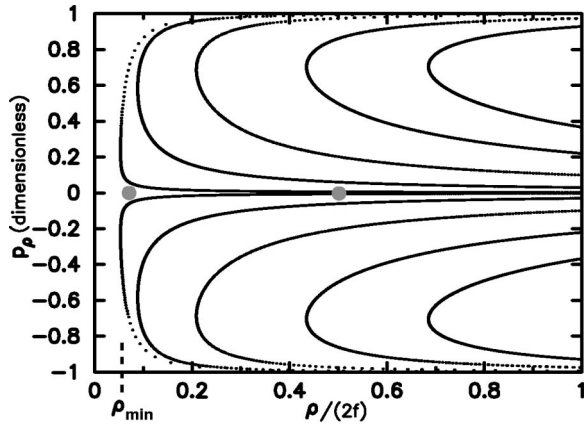
FIG. 11. Poincaré surface of section of the ray dynamics for $L_z = 0.1f$ as in Figs. 10(a)–10(c). The minimum distance ρ_0 from the z axis, given by Eq. (87), is indicated by the dashed line. All quasiperiodic trajectories fill smooth curves extending between some minimum $\rho_{min} \gtrless \rho_0$ and $\rho = 2f$. The two gray dots are the crossings of the focal plane generated by a periodic orbit, as shown in Fig. 10(a). The plot uses $2f$ as the length unit.

typical trajectory is—as mentioned above—quasiperiodic, and in the SOS generates a dense set of points that all lie on a smooth curve. Several trajectories have been followed in this way, and are represented in Fig. 11 by the different individual curves. Each curve exhibits some minimal axial distance $\rho_{min} > \rho_0$; this is a true inequality because quasiperiodic orbits do not reach their point of closest approach to the z axis precisely on the focal plane. Since the SOS record the instantaneous ρ upon crossing the focal plane, the resulting curves have their turning points at larger ρ.

The only orbits which have their real turning points exactly at the focal plane are the periodic orbits. A periodic orbit, as displayed in Fig. 10(a), generates exactly two discrete points in the SOS, corresponding to the two distinct values of the radial distance ρ at which the axis $z=0$ is crossed. Both points in the SOS lie at $p_\rho=0$ for the periodic orbit, as can be verified from the trajectory in the z-ρ plane which always crosses the z axis perpendicularly. The quasiperiodic trajectory of Fig. 10(b) corresponds to the leftmost curve in Fig. 11, which has its turning point almost at ρ_0 in the SOS. The caustic is almost on the focal plane, but still offset from it by an amount that is not discernible in Fig. 10(b).

The distinction between the periodic orbit and its closely neighboring quasiperiodic relative in the SOS of Fig. 11 is appreciable—a pair of points generated by the former, versus a one-dimensional curve for the latter. But exactly on the line $p_\rho=0$, there exists an infinite number of other pairs of points, belonging to the periodic orbits of the same family.

The SOS in these coordinates allow us to see directly in which places the focal plane comes into contact with the rays under consideration. This is a central piece of information when it comes to estimating the focusing at this plane where the quantum well is assumed to be. The forbidden regions around the z axis induced by the angular momentum barrier show up as inaccessible portions of the SOS toward small ρ.

F. Accuracy of the semiclassical approximation

We can also comment on the striking accuracy of the semiclassical approach in this system. The Poincaré section

shows that almost all trajectories (with the exception of the periodic paths) generate curves with the same topology: they begin and end at $\rho=2f$, with one turning point inbetween. There are other integrable systems for which the Poincaré section has a more complicated structure, one closely related example being the ellipsoidal cavity [22] or its two-dimensional counterpart, the ellipse billiard [23]. In this case, the phase space consists of two components in which the topology of the trajectories is different: One type of motion consists of rays circulating around the perimeter as so-called whispering-gallery orbits; the other is a bouncing-ball oscillation across the short diameter [24]. There is a division between these two types of trajectories, similar to that between oscillation and rotation in a pendulum—called the separatrix. The WKB approximation or its higher-dimensional generalization, named after Einstein, Brillouin, and Keller, cannot be applied without severe corrections in the vicinity of such a separatrix in phase space [25,22,23]. In our case, this breakdown never occurs, and semiclassical results are thus of high accuracy. Being a conic section, the parabola can of course be considered as a limiting case of the ellipse, with one of its foci moved to infinity. This leaves no possibility for bouncing-ball trajectories, which leads to the absence of a separatrix.

Finally, it is worth asking why the sharp corners at the intersection between the paraboloid and the focal plane do not cause any corrections to our semiclassical treatment, even though the surface curvature at these points is clearly much shorter than the wavelength. It is known that in such cases *diffraction* can occur, which makes it impossible to explain the mode structure purely based on classical orbits [26,27]. However, this phenomenon is absent for certain special angles subtended by the corners. One of these ''benign'' angles is precisely the 90° angle we encounter at the corners of the double paraboloid (cf. Fig. 3). When the confocal condition is violated, so that deviations from a right angle occur at the corners, we have to expect diffractive corrections to the semiclassical analysis, resulting from classical rays that hit the corners and are reflected in an arbitrary direction because the law of specular reflection is undefined in that instance. Fortunately, we shall see in Sec. VII that such orbits are far removed from the regions of phase space where we expect the important focusing modes to lie.

In this section, we have discussed how the ray dynamics develops a caustic structure, and how the latter can be represented with the help of the Poincaré section. We have also observed that the high-intensity regions in the wave solutions correspond to the ray caustics, because there the density of rays is high—in fact divergent if we recall the discussion of the classical turning points in the effective potential below Eq. (47). Therefore, even in situations where we cannot obtain the wave solutions easily, their possible intensity distribution can be inferred by investigating the ray dynamics first. This will now be carried out for a cavity that deviates from the ideal model shape.

VII. NONCONFOCAL DOUBLE PARABOLOID

Having obtained an overview of the types of ray motion that can be encounterd in the parabolic dome, and established the connection to the mode structure of the full vec-

torial wave equations via the short-wavelength approximation, we now want to introduce a model cavity for which the wave solutions cannot be obtained by separation of variables. The variety of possible deviations from the ideal model geometry of Fig. 3 is enormous, so we have to restrict attention to certain special distortions that can be expected to be generic in some sense.

A. Model deformation

The distortions we choose are obtained by pulling the two intersecting paraboloids in Fig. 3 apart or pushing them together along the z axis by an amount 2ϵ. Specifically, in spherical coordinates as a function of polar angle θ, the shape is given by

$$r(\theta) = \frac{2f}{1 + \cos\theta} + \frac{2\epsilon}{1 + \sqrt{1 + \epsilon(1 - \cos^2\theta)}}. \quad (91)$$

The respective foci, which coincide in the integrable model, then move off the ρ axis. This nonconfocal arrangement of the parabolic walls can be viewed as a model for fabrication-induced deviations from the ideal cavity shape—where the dome could be slightly too flat or too pointed. It can also be interpreted in a different way, taking into account the possibility that the boundary condition at the base of the dome is not exactly given by Eq. (7), if some penetration of the field through the dielectric mirror on the quantum well is taken into account. This is of course a realistic expectation, and its effect on the wave solutions would be that the TE electric field no longer needs to be strictly symmetric under reflection at the focal plane. If one maintains that the dome has indeed been fabricated with its base in the focal plane, this ''soft'' boundary condition on the mirror can be modeled by assuming that our solutions should correspond to waves reflected at a plane removed from the dielectric interface by some amount ϵ.

Therefore, the nonconfocal double paraboloid is a way of taking into account the cumulative effects of fabrication uncertainty and soft boundary conditions at the dielectric mirror with a single model parameter ϵ, denoting half the distance between the foci of the top and bottom parabolic wall in the unfolded cavity. One could think that a perturbation theory in ϵ could allow us to use the solutions obtained so far and smoothly extend them to the non-confocal situation. This is the traditional approach in physics and it is the reason why only simple, integrable systems are treated in textbooks on quantum mechanics or classical mechanics alike. However, perturbation approaches become tedious and even impossible for wave equations whose short-wavelength limit (i.e., ray picture) exhibits *chaotic dynamics*. The difficulties that arise can already be seen without introducing chaos, if we try to obtain the wave functions of an ellpsoid-shaped resonator as a perturbative expansion starting from the eigenfunctions of a spherical cavity. This poses no problems as long as one is interested only in modes of the ellipsoid whose topology is analogous to that found in the circle [28]. However, as mentioned earlier, the ellipsoid exhibits separatrix structure in phase because there exists a type of motion that the sphere does not possess: the bouncing-ball trajectories.
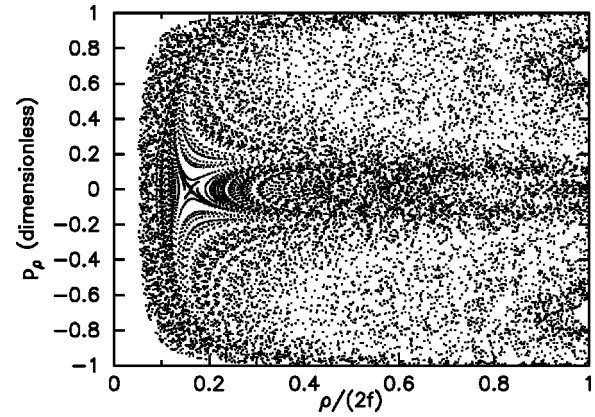
FIG. 12. Surface of section at $L_z = 0.1f$ of a nonconfocal double-paraboloid, with foci pulled apart by $\epsilon = 0.02f$. This destabilizes the cavity, leading to chaotic ray dynamics which generates an irregular cloud of points filling almost the whole region that is accessible for this L_z. A special point is encountered on the line $p_\rho = 0$, where the irregularity gives way to a confluence of hyperbolic traces whose vertices are centered on a single, unstable periodic orbit. The spatial pattern of this new periodic orbit is shown in Fig. 13(a).

Analogous *nonperturbative* effects arise in the present model, because the distortion can lead to new types of trajectories that are not present in the confocal cavity, in a process known as bifurcation [29,30]. The first consequence of the deformation ϵ is that the infinite families of periodic orbits break up, leaving only a distrete number of periodic orbits of the same topology, which can be divided in an equal number of stable and unstable paths. Stable paths have the property that rays with slightly different initial conditions remain close to the given periodic path for all times, while unstable periodic orbits are surrounded in their immediate neighborhood by chaos—trajectories deviate from such a periodic orbit at an exponential rate if the initial condition is only infinitesimally varied. For more quantitative statements and further background on the transition to chaos, the reader is referred to the literature [29,31,18].

B. Unstable and stable ray motion in the deformed cavity

The Poincaré section is very suitable as a diagnostic tool to identify this process of emerging chaos on on hand, and the stabilization of certain periodic orbits on the other hand. This is illustrated in Fig. 12. The perturbation consists of pulling the foci of the walls apart by $\epsilon = 0.02f$ along the z axis. Since this preserves the axial symmetry of the cavity, L_z is still a conserved quantity—the arguments of Sec. VI C rely on no other symmetries of the problem. We chose $L_z = 0.1f$ in the plot. The small distortion of 1% is already sufficient to change the phase space portrait significantly, compared to Fig. 11. The unstable periodic orbit (appearing prominently in Fig. 12 as a so-called hyperbolic point) is shown in its spatial pattern in Fig. 13(a). It is a self-retracing periodic orbit because it reflects from the boundary at normal incidence (in the z-ρ plane).

The effects that chaos can have on the ray motion are illustrated in Fig. 13(b). Shown here is a single ray trajectory which superficially has some similarity to Fig. 10(b). However, the path does not trace out a well-defined caustic in Fig.
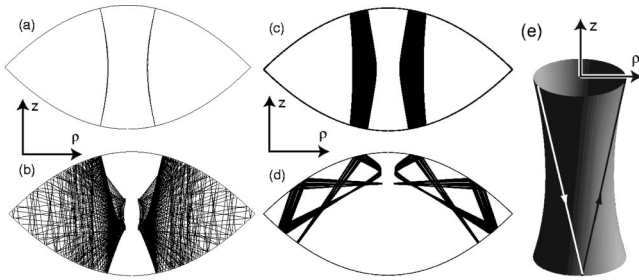
FIG. 13. Trajectories in the nonconfocal cavity. (a) shows the unstable periodic orbit arising at $\epsilon = 0.02f$, and $L_z = 0.1f$; cf. Fig. 12. For the same parameter, a chaotic trajectory is seen in (b). Oscillatory motion around stable periodic orbits occurs in (c) and (d), where $\epsilon = -0.02f$ and $L_z = 0.1f$, as in the SOS of Fig. 14. The patterns of type (a) and (c) derive from the periodic motion of Fig. 10(a) as a result of the shape perturbation. In real three-dimensional Cartesian space, (e) shows the straight-line ray motion (arrows) giving rise to the curved "envelope" surface, whose cross section we see in (a).

13(b). What looks like a caustic here is in fact better described as two caustics of the type in Fig. 10, arranged almost symmetrically with respect to the focal plane. Note, in particular, the symmetric occurrence of cusps both below and above the line $z = 0$. Recall that in the integrable case the positions ρ_0, and z_0 of the caustic singularity are uniquely given by the turning points ξ_0 and η_0 (or equivalently u_0 and v_0), in the effective potential. Reversing the sign of the cusp coordinate z_0 corresponds to *exchanging* the role of ξ and η. The significance of Fig. 13(b) is therefore that the degrees of freedom ξ and η are no longer decoupled, because during a single ray trajectory both the cusps at z_0 and $-z_0$ are reached. By virtue of Eq. (89), the quantity Z is thus not conserved any lomger. A trajectory is able to exhibit multiple points of closest approach to the z axis, and is not strictly guided by caustics.

Under these circumstances, it is not clear what to expect for the mode structure of the cavity, because we lose the possibility of labeling the eigenstates by a complete set of quantum numbers. This does not imply that there are no modes associated with chaotic rays, but one requires additional techniques to perform a semiclassical quantization [31,32]. The destruction of the conserved quantity Z means that there is one less constraint which the ray trajectories have to satisfy; this allows them to fill two-dimensional areas instead of one-dimensional curves in the SOS. Since the SOS gives us a picture of how rays intersect the plane $z = 0$, chaotic rays can be seen to show a less concentrated overlap with that plane. We anticipate that the presence of true caustics is required to create the best focusing action. With this hypothesis, the goal must be to identify ray orbits that exhibit caustics. This occurs in the vicinity of stable periodic orbits, due to the fact that perturbed trajectories execute an oscillatory and in general quasiperiodic motion around such stable orbits. In Fig. 12, however, no stable periodic orbits can be identified, telling us that, for the deformation chosen there, no stable modes with $L_z = 0.1f$ should exist.

The situation changes if we consider Fig. 14, in which L_z is the same but the sign of the nonconfocal displacement ϵ is reversed. The walls of the double paraboloid are hence pushed together instead of being pulled apart. The resulting
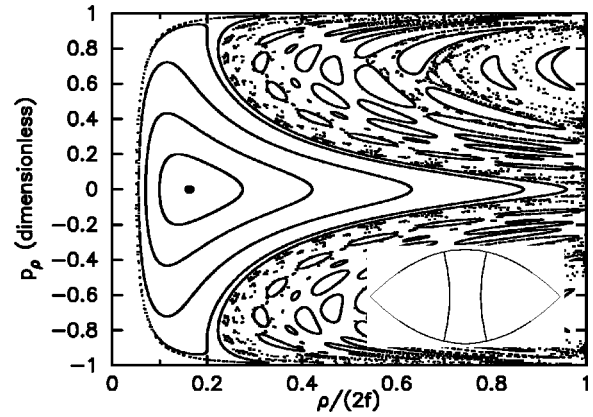

FIG. 14. Surface of section at $L_z = 0.1f$ with $\epsilon = -0.02f$. The cavity develops a multitude of stable periodic orbits surrounded by elliptical islands. The most prominent island of stability is centered on the the line $p_\rho = 0$ where a small circle indicates the location of the corresponding periodic orbit around which other trajectories can oscillate. Shown in the inset is the central stable periodic orbit. The next innermost closed line in the SOS belongs to the trajectory shown in Fig. 13(c).

phase space structure in the SOS differs markedly from Fig. 12: many trajectories trace out one-dimensional curves in the SOS which organize as closed loops, forming island chains that proliferate with various sizes. All these islands are centered around stable periodic orbits—the largest island of stability lies symmetrically around the line $z = 0$, and corresponds to oscillatory motion of the type shown in Fig. 13(c). The center of the island is in fact formed by a periodic orbit similar to Fig. 13(a), the only difference being that small perturbations of its initial conditions do not lead to chaos as in Fig. 12, but to the motion of Fig. 13(c).

Another oscillatory ray path centered at a stable periodic orbit is shown in Fig. 13(d). The pattern should be compared to Fig. 10(c), which has the same L_z. The similarity is apparent, except for the fact that the path in Fig. 10(c), will eventually fill the remaining gaps in that plot, if one follows it for a longer time. The path in Fig. 13(d), on the other hand, is truly restricted to the vicinity of a self-retracing orbit which reverses its propagation direction at one end due to perpendicular reflection at the wall, and at the other end by running up the centrifugal barrier perpendicular to the z axis.

All islands of stability in Fig. 14 generate their own caustics, which are topologically different from the ones in the integrable system. The caustic created by the orbit in Fig. 13(c) is simply the boundary of the regions into which the ray never penetrates. The difference between the absence and presence of caustics in Figs. 13(b) and 13(c) is not easily appreciated if we consider only the real-space plots. Here the usefulness of the Poincaré section as a diagnostic tool is again to be noted—showing two-dimensional clouds of points versus one-dimensional curves, respectively, for trajectories without and with caustics.

It follows from the preceding discussion that a negative ϵ leaves us with a cavity that is in many respects similar to the unperturbed double paraboloid [cf. the ray pattern of Fig. 13(d)]. However, the qualitative and important difference is that some periodic orbits are now *more stabilized* than at $\epsilon = 0$. In particular, there are simple ray bundles such as Fig.
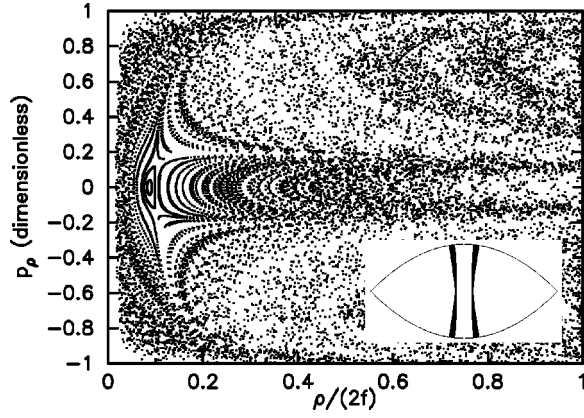
FIG. 15. For the same deformation $\epsilon = 0.02f$ as in Fig. 12, this surface of section at the smaller angular momentum $L_z = 0.03f$ shows that a stable orbit exists in addition to the unstable hyperbolic one. This is indicated by the elliptic (lens-shaped) island structure. The hyperbolic point is located to the right of the island. The ray pattern near the stable periodic orbit is shown in the inset. The small corresponding mode volume is apparent.

13(c) that promise reasonable focusing close to the center of the unfolded cavity. The physical explanation for the general stabilizing effect that we achieved by moving the paraboloids closer together lies in the well-known fact that a two-mirror resonator configuration has a focusing action when the mirrors are separated by less than the sum of their radii of curvature. Conversely, mirrors that are further apart than this criterium act in a defocusing way. This is consistent with the observation of a large chaotic domain in Fig. 12.

These simple arguments, and the chaotic picture of Fig. 12, seem to suggest that stable ray motion is not to be expected in the supposedly defocusing configuration with $\epsilon = 0.02f$. However, when applying the standard criteria for focusing and defocusing resonator geometries, we have to bear in mind that we are dealing with a centrifugal billiard whose ray trajectories are curved. The effect of the centrifugal barrier is to push the regions of allowed ray motion outward, until only a small patch surrounding the equatorial corners of the cavity is accessible. At large L_z the motion is then so confined that chaos does not develop. This is just the whispering-gallery phenomenon [17]. On the other hand, at $L_z = 0.1f$ we certainly found chaos with no remaining islands of stability. Small L_z's are what we must be interested in if concentration near the focal points is to be achieved.

In view of this, it is all the more surprising that the same cavity does in fact support stable orbits at even *smaller* angular momenta than in Fig. 12. This is shown in Fig. 15 for $L_z = 0.03f$. The periodic orbit responsible for the single stable island in that SOS is again almost identical to the one shown in Fig. 13(a), and its oscillatory neighborhood is analogous to Fig. 13(c); the inset of Fig. 15 shows this similarity. This stable orbit exists only at sufficiently small L_z; its associated island in the SOS shrinks to a point when $L_z \approx 0.038f$. The conclusion is that *both* the nominally focusing and defocusing configurations $\epsilon = \pm 0.02f$ permit the formation of ray bundles with a spatial distribution as in Fig. 13 (c), and hence the stable modes associated with this pattern should be robust. This is also confirmed by analogous Poincaré sections for larger displacements of the foci. At

larger $|\epsilon|$, motion of type shown in Fig. 13(c) and the inset of Fig. 15 is in fact stabilized further—for both directions of displacements *alike*.

The modes corresponding to this particular ray pattern are closely related to the fundamental s waves we discussed in Sec. III E, because both arise from ray bundles in the immediate vicinity of the *shortest* periodic orbits in the cavity. For $\epsilon = 0$ this was the family of paths in Fig. 10(a), members of which can be smoothly deformed into Fig. 13(a) without changing the topology— i.e., the number and sequence of reflections and turning points. we shall therefore call all these orbits the *fundamental orbits* of the cavity. The mode spacing of the corresponding eigenstates should also be comparable for the perturbed and unperturbed cases. However, we have to defer a detailed analysis of the wave solutions and their semiclassical correspondence to a future paper. Here, the goal has been to introduce the ray dynamics and its phase space as the backbone on which the mode structure is built.

Assuming that the deformation is $\epsilon = 0.02f$, we have the peculiar situation that the fundamental orbit is unstable if $L_z > 0.038f$, (cf. Fig. 12). Therefore, the most desirable modes will be those with smaller L_z. According to Eq. (78), we have to choose modes with low n and high k to achieve this. For the experimental cavity we have $kf \approx 14\pi$. Taking $n = 1$ as in Sec. III E, we arrive at the semiclassical value

$$L_z = \frac{f}{14\pi} \approx 0.023f, \qquad (92)$$

which is close to the situation depicted in Fig. 15. The difference in the SOS is insignificant. We have no accurate way of determining the actual value of ϵ most closely describing the real structure, but these considerations give us considerable confidence that modes with a spatial pattern as in Figs. 13(c) or 15 will be found in the cavity, because the relevant L_z estimated above is in a range where this fundamental orbit is stable—*irrespective* of the sign of ϵ and moreover largely independent of its magnitude.

VIII. BRAGG MIRROR AS AN ESCAPE WINDOW IN PHASE SPACE

The internal ray dynamics of the dome resonator has up to this point been evaluated under the assumption that the cavity is a perfect resonator. There are two physical mechanism that invalidate this viewpoint: absorption in the gold mirror, and transmission through the Bragg grating. The trade-off between the comparatively large absorption of a metal, on the one hand, and its ability to reflect omnidirectionally, on the other hand, were discussed in Ref. [33]. In our context, metallic absorption will always degrade the Q factor because the gold layer provides only an estimated 95% reflectivity [33]. However, the reflectivity of the Bragg mirror can be significantly *lower* for certain modes and in that case constitutes the dominant mechanism for Q spoiling. The variable that determines the reflectivity of the Bragg mirror (at the fixed operating frequency) is the *angle of incidence* χ with respect to the z axis. For purposes of a qualitative analysis, we assume that the Bragg reflectivity is unity for $\chi < 22°$ $\equiv \chi_c$, but drops to $\approx 20\%$ outside this cone of incidence
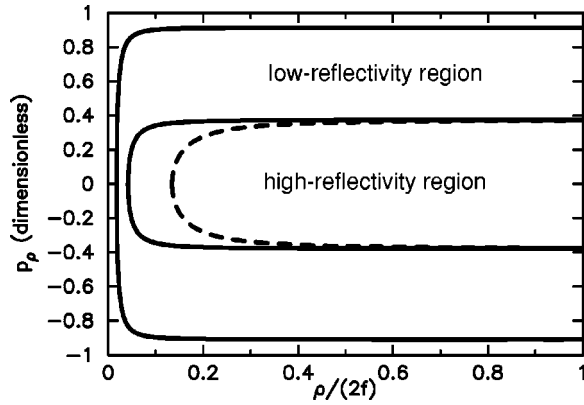
FIG. 16. Assuming that the Bragg mirror stack at the plane $z = 0$ yields high reflectivity only for waves within $\chi_c = 22°$ from the surface normal, or for regions of high reflectivity in the Poincaré section that are bounded by Eq. (96). The resulting curves bounded by $|p_\rho < 0.374$ are shown for $L_z = 0.03$ (solid line) and $L_z = 0.1$ (dashed line). A second high-reflectivity window exists for rays falling between the boundary of this plot and the solid line near the boundary. This becomes relevant only for the integrable confocal cavity, because the perturbed shapes have no stable orbits in this second window.

[33]. In other words, χ_c is the boundary between absorption-dominated and leakage-dominated Q factors. A second window of high reflectivity opens for rays at very oblique incidence on the grating surface, more specifically for $\chi > 60°$. This second window will be discussed further below.

The ray picture allows us to use this rough transmission criterion as a guide in order to separate long-lived cavity modes from short-lived ones. The angle χ between z axis and a trajectory is, according to Eq. (72), given by

$$\cos \chi = \dot{\mathbf{r}} \cdot \mathbf{e}_z = \dot{z}, \tag{93}$$

so that

$$1 - \dot{z}^2 = \sin^2 \chi. \tag{94}$$

One can substitute this as the right-hand side of Eq. (83), and obtain an equation for a curve in the plane $\dot{\rho}, \rho$ ($\dot{\rho} = p_\rho$) spanning the Poincaré section:

$$|p_\rho| = \sqrt{\sin^2 \chi - \frac{L_z^2}{\rho^2}}. \tag{95}$$

Using the critical value of χ_c in this equation specifies the escape condition in the Poincaré section: the Bragg mirror becomes ineffective when

$$|p_\rho| > \sqrt{\sin^2 \chi_c - \frac{L_z^2}{\rho^2}}. \tag{96}$$

In order to obtain a feeling for the type of ray orbits that can remain in the cavity under this escape condition, in Fig. 16 we plot the resulting curves in the surface of section for the two different values of L_z appearing in Figs. 11, 12, 14, and 15. The plot should be superimposed on these plots to decide which parts of the respective phase space falls within

the high-reflectivity range of the DBR grating. Note that the critical lines for ray escape are independent of deformation because they rely only on Eq. (83).

As a result of this comparison, we find first of all that low angular momenta are required by the escape criterion, because the phase-space area enclosed by the critical curves in Fig. 16 shrinks with increasing L_z. This is understandable because the ray motion in this case has a strong azimuthal component contributing to the tilt angle with respect to the z axis. Let us turn our attention to the stable periodic orbits arising in the chaotic Poincaré sections. The case $L_z = 0.1f$, shown previously for illustrative purposes, now turns out to be roughly the maximum angular momentum at which the stable orbit of Fig. 14 is still confined by Bragg reflection. The lower angula momentum $L_z = 0.03f$ coming close to the estimated value for the s waves of our experimental cavity, on the other hand, places the stable periodic orbit well inside the high-reflectivity range of the DBR. For the case of a defocusing deformation this is illustrated in Fig. 15. The periodic point is at $\rho \approx 0.086$. For a focusing deformation of the same magnitude, $\epsilon = -0.02$, the periodic point lies at $\rho \approx 0.99$. Both values are to the right of the solid line in Fig. 16, corresponding to high reflectivity.

For the *chaotic* orbits, we observe that they spread out over the Poincaré section in such a way as to yield significant overlap with the low-reflectivity regions of Fig. 16. This is true for all Poincaré sections shown in this paper. Therefore, we conclude that *cavity modes associated with the chaotic phase space regions are short lived*, and the corresponding broad resonances will not affect the spontaneous emission enhancement of the parabolic dome. A quantitative estimate of the resonance lifetimes could be obtained by measuring the time that a chaotic trajectory spends, on average, in the high-reflectivity region, without excursions beyond the critical line. However, we shall not attempt quantitative predictions at this stage of our investigation, and defer it to future work.

A quantitative analysis would also be necessary to determine the modal lifetimes in the marginal case of the ideal *confocal* cavity. The reason is that the ray picture alone does not allow a clear distinction between classically confined and unconfined orbits, because the classification according to stable and unstable trajectories does not apply in the integrable parabolic dome. All the solid curves in the Poincaré section of Fig. 11 cross into the low-reflectivity region of Fig. 16 at some point, but the time spent in the high-reflectivity range can be very long classically. To illustrate this, in Fig. 17 we show a particular ray trajectory for $L_z = 0.1f$ in the confocal paraboliod, which for almost 500 crossings of the focal plane remains inside the regions of high reflectivity. This time, the second window of high reflectivity close to the border of the SOS is important because the ray alternates between the low- and high-χ windows from one crossing of the focal plane to the next. The regular nature of this motion makes long lifetimes possible because it strictly prevents the ray from entering the low-reflectivity region for long times, whereas a chaotic orbit would quickly explore this domain in a quasirandom way.

The trajectory shown in Fig. 17 is practically identical to the one shown in Fig. 10(b). The alternating way of intersecting the focal plane can be understood from that figure, or
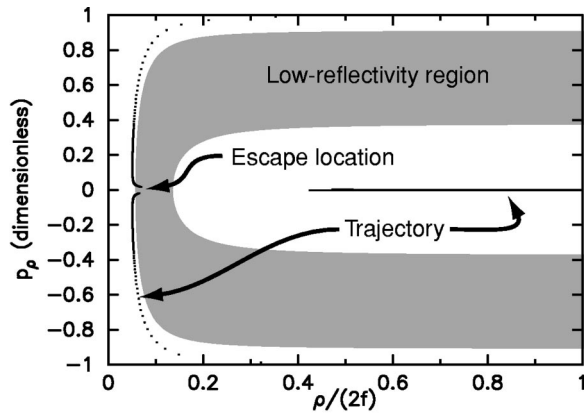
FIG. 17. The Poincaré section combined with the escape conditions can be used to extract information about the lifetime and escape locations. This is illustrated here for a single ray orbit (black trace), followed for 500 crossings of the focal plane. The gray area is the region which has to be avoided by the ray in order to remain in the cavity.

from Fig. 10(a), which shows periodic orbits closely neighboring the quasiperiodic trajectory of plot (b). Note that the ray model allows us, in addition, to predict the spatial location where the mode corresponding to this ray bundle will preferentially be coupled out through the Bragg mirror. As can be seen in Fig. 17, the low-reflectivity region is reached for the first time when, after many reflections, the trajectory departs from the immediate neighborhood of the focal region, i.e., intersects the focal plane with a ρ that is slightly too large.

The subtle balance of parameters that prevents chaos from appearing will, in all experimental realizations, be shifted to either the defocusing or the focusing side. Therefore, the above ray analysis of the mixed phase spaces for these two situations above is our main concern. However, as in previous sections the integrable case is a useful starting point to illustrate our strategy. The advantage of the ray approach is that it provides fast and intuitive predictions, but further studies are required in order to determine how this model succeeds in characterizing the cavity quantitatively. Paradoxically, we can already conclude that the existence of chaos and islands of stability makes it easier to obtain results from a ray analysis, because there is a sharper separation between long lifetimes for the stable modes discussed above and short lifetimes for modes associated with the chaotic portions of the SOS.

IX. CONCLUSION

In this paper we have examined the modal structure of the electromagnetic field in a semiconfocal planoparabolic cavity (or, equivalently, in a double-paraboloid confocal cavity) in view of our recent fabrication of semiconductor microcavities having that geometry. In order to account for the effects of the inevitable fabrication defects, we also considered the stability of the modes with respect to deformations consisting of deviations with respect confocality. This theoretical analysis was thus motivated by our ongoing experiments on these structures, and feeds back into this experimental work by opening an interesting perspective in terms

of investigating the chaotic structure and dynamics of some of the modes of cavity.

Regarding the structure of the modes in the parabolic cavity, we note that the scalar wave equation is solvable analytically by separation of variables. However, the vectorial boundary conditions for the electromagnetic field destroy this property, leaving only the cylindrical symmetry. Nevertheless, the fundamental series of s waves (free of azimuthal nodes) in a confocal electromagnetic cavity can be solved rigorously. It has its energy concentrated in a small volume (of order λ^3) around the focal point, even though at the focal point itself the electric field is zero due to the vectorial nature of the field. The higher order modes cannot be solved as readily in the full three-dimensional model, but it is possible to appreciate their features by reducing the problem to scalar form. In these higher order modes, the energy is concentrated in lobes that surround the focal point, but avoid it because of the centrifugal barrier that arises from the cylindrical symmetry. Indeed, these modes correspond to non-zero values of the angular momentum ($m \neq 0$) and for large values of m tend toward a type of whispering-gallery modes with intensity concentrated in a ring along the focal plane, [cf. Fig. 10(d)].

The stability of the modes of the parabolic cavity with respect to geometrical deformations can be assessed by examining the ray trajectories that correspond to each mode. For a deformation that corresponds to a small deviation from confocality, chaotic ray patterns emerge. However, we also find stable ray orbits concentrated in a small part of the cavity volume. Independent of deformation, the most important stable orbits are those which in cylinder coordinates ρ and z follow the shortest possible periodic trajectory. This general topology is the same for a range of deformations (including the ideal confocal cavity), and corresponds to a ray returning to the same ρ and z after two reflections, missing the focal point by a small amount because the field there has to vanish. The generic shape of this orbit is represented in Fig. 13, and its special modification in the confocal case with its marginal stability is shown in Fig. 10. The topological equivalence between the stable orbits of the distorted cavity, on the one hand, and of the confocal system, on the other hand, indicates that the structure of the fundamental s wave is stable with respect to deformations.

From an experimental viewpoint, the results of this theoretical analysis indicate that the cavities already fabricated in our laboratory should possess stable modes in which the energy is confined in a volume of order λ^3 in the vicinity of the focal point, in spite of fabrication errors. The higher order modes, in which the field is concentrated away from the focal point, in whispering-gallery-type configurations, will be unstable because of the presence of fabrication defects. At the same time these modes will decay quickly fast as they correspond to oblique incidences onto the Bragg mirror, at angles for which the mirror is no longer reflecting. Experiments are in progress to characterize the structure and dynamics of both the stable and unstable modes [7]. The robust stable modes in which the field is confined in the vicinity of the focal point should give rise to a strong enhancement of the spontaneous emission of a dipole (such as a semiconductor quantum well or a semiconductor quantum box) placed there, and a concomitant lowering of the lasing threshold,

even for our cavities that are of mesoscopic dimensions. This is because because even in such large cavities, whose geometric volume is of the order of a few thousand cubic wavelengths, the central lobe of the fundamental *s* wave (which contains most of the energy) has an effective volume of the order of one cubic wavelength.

These considerations underscore the interest that parabolic microresonators present by exhibiting quantum electrodynamic effects as well as optical chaos, in spite of their relatively large dimensions. In addition, the mesoscopic cavity dimensions of these structures are an important practical feature, as they make the fabrication accessible to existing experimental techniques (such as focused ion beam etching) while, at the same time, they greatly facilitate the theoretical analysis of these devices as they permit the use of short-wavelength approximations.

APPENDIX: PARABOLIC COORDINATES

The parabolic coordinates ξ, η, and ϕ are related to the three-dimensional Cartesian coordinates according to

$$x = \sqrt{\xi\eta}\cos\phi,$$

$$y = \sqrt{\xi\eta}\sin\phi, \tag{A1}$$

$$z = \tfrac{1}{2}(\xi - \eta),$$

or, equivalently,

$$\xi = r + z,$$

$$\eta = r - z, \tag{A2}$$

$$\phi = \arctan\frac{y}{x},$$

where $r = \sqrt{x^2 + y^2 + z^2}$ is the spherical radius vector. With this definition, ξ and η have the same dimensions as the Cartesian coordinates, which is helpful for physical considerations. The surfaces $\xi = $ const are paraboloids by revolution about the positive $\hat{z}$ axis having their focal point at the origin, while the surfaces $\eta = $ const are directed along the negative $\hat{z}$ axis. The plane $z = 0$ corresponds to the condition $\xi = \eta$. In terms of the cylindrical coordinates $\rho = \sqrt{x^2 + y^2}$, z, and ϕ, the parabolic coordinates obey

$$\rho = \sqrt{\xi\eta},$$

$$z = \tfrac{1}{2}(\xi - \eta) \tag{A3}$$

and

$$\hat{\rho} = \frac{1}{\sqrt{\xi + \eta}}(\sqrt{\eta}\cdot\hat{\xi} + \sqrt{\xi}\cdot\hat{\eta}),$$

$$\hat{z} = \frac{1}{\sqrt{\xi + \eta}}(-\sqrt{\xi}\cdot\hat{\xi} + \sqrt{\eta}\cdot\hat{\eta}). \tag{A4}$$

In these parabolic cordinates, the electric field $E = (E_\xi, E_\eta, E_\phi)$ is related to its representation in cylindrical coordinates according to

$$\vec{E} = \begin{cases} E_\xi = \sqrt{\dfrac{\eta}{\xi + \eta}}\dfrac{i}{\sqrt{2}}(E_+ - E_-) - \sqrt{\dfrac{\xi}{\xi + \eta}}E_z \\[2mm] E_\eta = \sqrt{\dfrac{\xi}{\xi + \eta}}\dfrac{i}{\sqrt{2}}(E_+ - E_-) + \sqrt{\dfrac{\eta}{\xi + \eta}}E_z \\[2mm] E_\phi = \dfrac{1}{\sqrt{2}}(E_+ + E_-). \end{cases} \tag{A5}$$

[1] R.E. Slusher and C. Weisbuch, Solid State Commun. **92**, 149 (1994).

[2] G. Björk, S. Machida, Y. Yamamoto, and K. Igeta, Phys. Rev. A **44**, 669 (1991).

[3] S.L. McCall, A.F.J. Levi, R.E. Slusher, S.J. Pearton, and R.A. Logan, Appl. Phys. Lett. **60**, 289 (1992).

[4] L. Collot, V. Lefèvre-Seguin, M. Brune, J.M. Raimond, and S. Haroche, Europhys. Lett. **23**, 327 (1993).

[5] D.J. Heinzen, J.J. Childs, J.E. Thomas, and M.S. Feld, Phys. Rev. Lett. **58**, 1320 (1987).

[6] F.M. Matinaga, A. Karlsson, S. Machida, Y. Yamamoto, T. Suzuki, Y. Kadota, and M. Ikeda, Appl. Phys. Lett. **62**, 443 (1993).

[7] I. Abram (unpublished).

[8] The focused ion beam etching process was carried out by Orsay Physics S.A. under contract.

[9] A.E. Siegman, *Lasers* (University Science Books, Mill Valley, CA, 1986).

[10] H. Laabs and A.T. Friberg, IEEE J. Quantum Electron. **35**, 198 (1999).

[11] M. Kerker, *The Scattering of Light and Other Electromagnetic Radiation* (Academic Press, New York, 1969).

[12] R. Balian and C. Bloch, Ann. Phys. (N.Y.) **60**, 401 (1970); **64**, 271 (1971).

[13] *Handbook of Mathematical Functions*, edited by M. Abramovitz and I.A. Stegun, (Dover, New York, 1972).

[14] J. Mathews and R.L. Walker, *Mathematical Methods of Physics*, (Addison-Wesley, Reading, MA, 1970).

[15] The first derivative can in principle be removed by another substitution of variables, $\rho = -\ln u$. All quantities entering the WKB procedure are, however, unchanged by this substitution. Therefore, the following discussion retains u as the variable.

[16] Y. Yamamoto and R.E. Slusher, Phys. Today **46** 6, 66 (1993), and references therein.

[17] H. Weyl, J. Reine Angew. Math. **143**, 177 (1913); Bull. Am. Math. Soc. **56**, 115 (1950).

[18] J.U. Nöckel and A.D. Stone, in *Optical Processes in Micro-cavities*, edited by R.K. Chang and A.J. Campillo (World Scientific, Singapore, 1996).

[19] C. Gmachl, F. Capasso, E.E. Narimanov, J.U. Nöckel, A.D. Stone, J. Faist, D.L. Sivco, and A.Y. Cho, Science **280**, 1556 (1998).

[20] J.U. Nöckel, A.D. Stone, and R.K. Chang, Opt. Lett. **19**, 1693 (1994).

[21] J.U. Nöckel and A.D. Stone, Nature (London) **385**, 45 (1997).

[22] P.H. Richter, A. Wittek, M.P. Kharlamov, and A.P. Kharlamov, Z. Naturforsch., A: Phys. Sci. **50a**, 693 (1995); H. Waalkens, J. Wiersig, and H. Dullin, Ann. Phys. (N.Y.) **267**, 64 (1999).

[23] H. Waalkens, J. Wiersig, and H. Dullin, Ann. Phys. (N.Y.) **260**, 50 (1997).

[24] J.B. Keller and S.I. Rubinow, Ann. Phys. (N.Y.) **9**, 24 (1960).

[25] R. Arvieu, F. Brut, J. Carbonell, and J. Trouchard, Phys. Rev.

A **35**, 2389 (1987).

[26] P.J. Richens and M.V. Berry, Physica D **2**, 495 (1981).

[27] J.B. Keller, J. Opt. Soc. Am. **52**, 116 (1962); M. Sieber, N. Pavloff, and C. Schmit, Phys. Rev. E **55**, 2279 (1997).

[28] L.D. Landau and E.M. Lifshitz, *Quantenmechanik* (Akademie-Verlag Berlin, 1979).

[29] L.E. Reichl, *The Transition to Chaos* (Springer-Verlag, Berlin, 1992).

[30] M. Brack and R. K. Bhaduri, *Semiclassical Physics*, Frontiers in Physics Vol. **96** (Addison-Wesley, Reading, MA, 1997).

[31] M.C. Gutzwiller, *Chaos in Classical and Quantum Mechanics* (Springer, New York, 1990).

[32] M.S. Child, *Semiclassical Mechanics with Molecular Applications* (Clarendon Press, Oxford, 1991), p. 189.

[33] I. Abram, I. Robert, and R. Kuszelewicz, IEEE J. Quantum Electron. **34**, 71 (1998).